1 # Urbanization-induced urban heat island and aerosol effects on

2 # climate extremes in the Yangtze River Delta Region of China

3 Shi Zhong[1, 2], Yun Qian[2*], Chun Zhao[2, 6], Ruby Leung[2], Hailong Wang[2], Ben Yang[3, 2], Jiwen

4 Fan[2], Huiping Yan[4, 2], Xiu-Qun Yang[3], and Dongqing Liu[5]

6 [1] State Key Laboratory of Hydrology-Water Resources and Hydraulic Engineering, Center for

7 Global Change and Water Cycle, Hohai University, Nanjing, China

8 [2] Pacific Northwest National Laboratory, Richland, WA, USA

9 [3] School of Atmospheric Sciences, Nanjing University, Nanjing, China

10 [4] College of Atmospheric Science, Nanjing University of Information & Technology, Nanjing,

11 China

12 [5] Nanjing Meteorological Bureau, Nanjing, China

13 [6] University of Science and Technology of China, Hefei, China

15 Corresponding author: Yun Qian [Yun.Qian@pnnl.gov]

17 Submitted to *Atmospheric Chemistry and Physics*

18 October 1, 2016

20   **Abstract**

21   The WRF-Chem model coupled with a single-layer Urban Canopy Model (UCM) is

22   integrated for 5 years at convection-permitting scale to investigate the individual and combined

23   impacts of urbanization-induced changes in land cover and pollutants emission on regional climate

24   in the Yangtze River Delta (YRD) region in eastern China. Simulations with the urbanization

25   effects reasonably reproduced the observed features of temperature and precipitation in the YRD

26   region. Urbanization over the YRD induces an Urban Heat Island (UHI) effect, which increases

27   the surface temperature by 0.53 °C in summer and increases the annual heat wave days at a rate of

28   3.7 d/yr in the major megacities in the YRD, accompanied by intensified heat stress. In winter, the

29   near-surface air temperature increases by approximately 0.7 °C over commercial areas in the cities

30   but decreases in the surrounding areas. Radiative effects of aerosols tend to cool the surface air by

31   reducing net shortwave radiation at the surface. Compared to the more localized UHI effect,

32   aerosol effects on solar radiation and temperature influence a much larger area, especially

33   downwind of the city-cluster in the YRD.

34   Results also show that the UHI increases the frequency of extreme summer precipitation

35   by strengthening the convergence and updrafts over urbanized areas in the afternoon, which favor

36   the development of deep convection. In contrast, the radiative forcing of aerosols results in a

37   surface cooling and upper atmospheric heating, which enhances atmospheric stability and

38   suppresses convection. The combined effects of the UHI and aerosols on precipitation depend on

39   synoptic conditions. Two rainfall events under two typical but different synoptic weather patterns

40   are further analyzed. It is shown that the impact of urban land-cover and aerosols on precipitation

41   is not only determined by their influence on local convergence, but also modulated by large-scale

42   weather systems. For the case with a strong synoptic forcing associated with stronger winds and

43 larger spatial convergence, the UHI and aerosol effects are relatively weak. When the synoptic

44 forcing is weak, however, the UHI and aerosol effects on local convergence dominate. This

45 suggests that synoptic forcing plays a significant role in modulating the urbanization-induced land-

46 cover and aerosol effects on individual rainfall event. Hence precipitation changes due to

47 urbanization effects may offset each other under different synoptic conditions, resulting in little

48 changes in mean precipitation at longer time scales.

1. Introduction

Urbanization affects climate and hydrological cycle by changing land cover and surface albedo, which releases additional heat to the atmosphere, and by emitting air pollutants, which interact with clouds and radiation (e.g., Shepherd, 2005; Sen Roy and Yuan, 2009; Yang et al., 2011). The most discernible impact of urban land-use change is the urban heat island (UHI) effect that can result in a warmer environment over urban areas than the surrounding areas (Landsberg, 1981; Oke, 1987). In addition to the thermal perturbations, the UHI has been well documented to modify wind patterns (Hjemfelt, 1982), evaporation (Wienert and Kuttler, 2005), atmospheric circulations (Shepherd and Burian, 2003; Baik et al., 2007; Lei et al., 2008), and precipitation around urban areas (Braham, 1979; Inoue and Kimura, 2004). Previous studies have found an increase of warm-season precipitation over and downwind of major cities due to the expanded urban land cover (Huff and Changnon, 1972; Changnon, 1979; Zhong et al., 2015). Recent studies suggested that the underlying urban surface also affects the initiation and propagation of storms (Bornstein and Lin, 2000; Guo et al., 2006) and convective activities in city fringes (Baik et al., 2007; Shepherd et al., 2010).

Concurrently increases in population and anthropogenic activities over urbanized areas increase pollutant emissions and aerosol loading in the atmosphere. Atmospheric aerosols have long been recognized to affect surface and top of the atmosphere (TOA) radiative fluxes and radiative heating profiles in the atmosphere via aerosol-radiation interactions (ARI) (e.g., Coakley et al., 1987; Charlson et al., 1992; Hansen et al., 1997; Yu et al., 2006; Qian et al., 2006, 2007, 2015; McFarquhar and Wang, 2006), which tend to induce cooling near the surface and heating at the low and mid-troposphere (Qian et al., 2006; Bauer and Mennon, 2012). Anthropogenic aerosols can also affect clouds and precipitation via aerosol-cloud interactions (ACI) (e.g., Rosenfeld, 2000,

79 2008; Qian et al., 2010; Fan et al., 2013; 2015; Tao et al., 2012; Zhong et al., 2015). Localized

80 changes in precipitation by strong aerosol perturbations can induce cold pools by evaporation,

81 which may alter the organization of stratocumulus clouds (e.g., Wang and Feingold, 2009;

82 Feingold et al., 2010). Aerosol impacts on deep convective clouds are complicated by the

83 interactions among dynamical, thermodynamical, and microphysical processes. For example, deep

84 convection could be invigorated by aerosols as more cloud water associated with the smaller cloud

85 drops is carried to higher levels where it freezes and releases more latent heat in a polluted

86 environment (Rosenfeld, 2008; Khain, 2009; Storer and van den Heever, 2013). Fan et al. (2013)

87 revealed a microphysical effect of aerosols from reduced fall velocity of ice particles that explains

88 the commonly observed increases in cloud top height and cloud cover in polluted environments.

89 Therefore, urbanization may influence precipitation and circulation through multiple pathways

90 that are more difficult to disentangle than the dominant effect on temperature.

91   As one of the most developed regions in China, the Yangtze River Delta (YRD) has been

92 experiencing rapid economic growth and intensive urbanization process during the past three

93 decades. With the highest city density and urbanization level in China, the YRD has become the

94 largest adjacent metropolitan areas in the world. It covers an area of 9.96×10^4 km^2, with a total

95 urban area of 4.19×10^3 km^2 (Hu et al., 2009). Observations have shown that the urban land-use

96 expansion in this region has induced a remarkable warming due to the significant UHI effect (Du

97 et al., 2006; Wu and Yang 2012, Wang et al., 2015). The annual mean warming reached up to

98 0.16°C/10yr based on station measurements in large cities (Ren et al., 2008), which accounted for

99 47.1% of the overall warming during the period of 1961-2000. Urbanization in the YRD was found

100 to destabilize the atmospheric boundary layer (Zhang et al., 2010) and enhance convection and

101 precipitation (Yang et al., 2012, Wan et al., 2013). Meanwhile, human activities associated with

102 the ever-growing population have led to a dramatic increase in air pollutant emissions (Wang et

103 al., 2006). Several observational and numerical studies have revealed that additional aerosol

104 loading in this region could reduce solar radiation reaching the surface (Che et al., 2005; Qian et

105 al., 2006, 2007), modify warm cloud properties (Jiang et al., 2013), and suppress light rainfall

106 events (Qian et al., 2009).

107   The individual effects of urbanization-induced UHI and aerosol emission on local and

108 regional climate have been examined separately in several modeling studies using short

109 simulations of selected weather episodes at high spatial resolution or multiple-year climate

110 simulations at coarse resolution. To more robustly quantify the urbanization-induced UHI and

111 aerosol effects, convection-permitting simulations may reduce uncertainties in representing

112 convection and its interactions with aerosols, which are parameterized in coarse-resolution models.

113 Additionally, multi-year simulations are needed to understand and quantify the overall effects of

114 land-cover change and aerosols in different large-scale environments (Oleson et al., 2008). In this

115 study, a state-of-the-art regional model coupled with online chemistry (WRF-Chem) and a single-

116 layer Urban Canopy Model (UCM) is used to simulate climate features in the YRD region. The

117 climatic effects of the separate and combined land-cover and aerosol changes induced by

118 urbanization are investigated using a set of 5-year (2006-2010) simulations with a horizontal

119 resolution at convection-permitting scale (3 km). The paper is organized as follows. Section 2

120 describes the model configuration, experiment design, and model evaluation. The urbanization

121 effects on extreme temperature and precipitation are presented in Section 3, followed by a

122 summary of the conclusions in Section 4.

123

2. Method

2.1 Model configuration

The WRF-Chem model (Grell et al., 2005; Fast et al., 2006; Qian et al., 2010) simulates trace gases, aerosols and meteorological fields interactively (Skamarock et al., 2008; Wang et al., 2009), including aerosol-radiation interactions (Zhao et al., 2011, 2013a) and aerosol-cloud interactions (Gustafson et al., 2004). The coupled single-layer UCM (Kusaka et al., 2001; Chen et al., 2001) is a column model that uses a simplified geometry with two-dimensional, symmetrical street canyons to represent the momentum and energy exchanges between the urban surface and the atmosphere. The RADM2 (Regional Acid Deposition Model 2) gas chemical mechanism (Stockwell et al., 1990) and the MADE (Modal Aerosol Dynamics Model for Europe) and SORGAM (Secondary Organic Aerosol Model) aerosol module (Schell et al., 2001) are used. Detailed configuration of the above models can be found in Zhao et al. (2010). No cumulus parameterization is used at the convection-permitting resolution. The physical parameterization schemes used in our simulations are listed in Table 1.

2.2 Numerical experiments

Simulations are performed over a model domain centered at (120.50 °E, 31.00 °N) with a horizontal grid spacing of 3 km and 50 vertical levels extending from the surface to 50 hPa. The lowest 10 model layers are placed below 1 km to ensure a fine vertical resolution within the planetary boundary layer. Initial and boundary conditions for meteorological fields are derived from the National Center for Environmental Prediction (NCEP) FNL global reanalysis data on 1° × 1° grids at 6-hour interval. Lateral boundary conditions for chemistry are provided by a quasi-

145 global WRF-Chem simulation (Zhao et al., 2013b) that includes aerosols transported from regions

146 outside the model domain.

147 The dominant land cover within each model grid cell is derived from the U.S. Geological

148 Survey (USGS) 30 second dataset that includes 24-category land-use type, except that the land use

149 over urban areas is updated using the stable nighttime light product (version 4) at 1 km spatial

150 resolution (available at the National Geophysical Data Center,

151 http://ngdc.noaa.gov/eog//dmsp/downloadV4composites.html). Corresponding to the value of

152 lighting index of 25-50, 50-58, and >58 in the above product, each urban grid is identified as "Low

153 Intensity Residential (LIR)", "High Intensity Residential (HIR)", or

154 "Commercial/Industrial/Transportation (CIT)", respectively. Figures 1a and 1b illustrate the urban

155 area within the model domain for year 1970 and 2006, respectively. The anthropogenic heating

156 (AH), characterized by a diurnal cycle with two peaks at rush hours of 0800 and 1700 LST,

157 respectively, is incorporated in the model simulations. The default maximum values of AH in WRF

158 for LIR (20 W m^{-2}), HIR (50 W m^{-2}) and CIT (90 W m^{-2}) are used in this study (Tewari et al.,

159 2007). Anthropogenic emissions of aerosols and their precursors are obtained from the Asian

160 emission inventory (Zhang et al., 2009b), which is a 0.5° × 0.5° gridded dataset for 2006. Black

161 carbon (BC), organic matter (OM), and sulfate emissions over China are extracted from the China

162 emission inventory for 2008 (Lu et al., 2011), which provides monthly mean data on 0.1° × 0.1°

163 grids. It should be noted that the Noah land surface model defines a dominant land cover type for

164 each grid, so no subgrid variability is simulated.

165 The anthropogenic emission fluxes of SO_2 and BC in the simulation domain are shown in

166 Figures 1c and 1d, respectively. Areas with large emissions are mainly located in four city clusters,

167 i.e., Nanjing-Zhenjiang-Yangzhou, Suzhou-Wuxi-Changzhou, Shanghai, and Hangzhou Bay, all

168   inside the mega-city belt. Biomass burning emissions for the simulation period are obtained from

169   the monthly Global Fire Emissions Database Version 3 (GFEDv3), which provides monthly mean

170   data on $0.5° × 0.5°$ grids and the vertical distribution is determined by the injection heights

171   described by Dentener et al. (2006) for the Aerosol Inter-Comparison project (AeroCom). Sea salt

172   and dust emissions are configured following the same approach of Zhao et al. (2013b).

173   In order to investigate the individual responses of local and regional climate to land-cover

174   change and increased aerosol loading, three experiments (i.e., LU06E06, LU70E70, and

175   LU70E06) are conducted for 5 years from 2006 to 2010. The configurations of land use and aerosol

176   emissions for these experiments are summarized in Table 2. All three simulations are performed

177   using the same initial and boundary conditions and physics schemes, but with different land use

178   types and/or anthropogenic emissions. LU06E06 is the control experiment, which represents the

179   "present" (2006) urbanization level for both land use and aerosol/precursor emissions. LU70E06

180   uses the present aerosol emission data but with the land use of the 1970s, which is derived from

181   the USGS dataset without the nighttime light correction. In LU70E70, both land use and emissions

182   are set to the conditions of the 1970s. The differences of LU06E06-LU70E06, LU70E06-

183   LU70E70, and LU06E06-LU70E70 can be used to derive the urban land-use effect, aerosol effect,

184   and their combined effect, respectively (Table 3). The simulations are initialized on December 15

185   of each year during 2005-2009 to allow for a 16-day spin-up time and then continuously integrated

186   for the next year (from January 1 to December 31). Results from January 1 to December 31 of all

187   five years (2006-2010) are analyzed.

188   **2.3 Model evaluation**

189   The surface skin temperature simulated in LU06E06 is averaged over 2006-2010 and

190   compared with the MODIS data. A spatial filtering method described by Wu and Yang (2012) is

191   applied to isolate the heterogeneous climatic forcing of urbanization. More specifically, for each

192   grid a spatial anomaly is defined as the departure from the average value over a region centered at

193   each grid. Then, the moving spatial anomalies are calculated for all the grids with the moving

194   region acting as a filtering window, which has a size of $1° \times 1°$. Figure 2 shows the moving spatial

195   anomalies of mean surface skin temperature from MODIS observations and the L06E06

196   simulation. The simulation captures the spatial distribution of observed surface skin temperature

197   very well. In particular, the warmer centers over highly urbanized areas are well reproduced,

198   despite slight underestimations in some mega cities in Zhejiang Province such as Hangzhou and

199   Ningbo. Shanghai and Su-Xi-Chang exhibit the highest temperatures that are 2 °C above the

200   surrounding rural areas.

201   To further validate the model, the baseline simulation LU06E06 is evaluated against

202   meteorological station observations for 2006-2010. Figure 3 shows the averaged near-surface

203   temperature and precipitation from observations and LU06E06. The simulated spatial pattern of

204   near-surface air temperature agrees well with observations, with high temperature centers located

205   at meteorological stations in major cities such as Shanghai and Hangzhou. The simulated

206   temperature displays substantial spatial variability associated with heterogeneity in topography,

207   land cover, and other regional forcings. The model captures the general north-to-south gradient of

208   increasing precipitation in the observations. However, the model overestimates precipitation in

209   Shanghai and central Jiangsu Province but underestimates the precipitation in the southwestern

210   part of the domain.

211

3. Results

3.1 Urbanization impact on surface temperature, radiation flux and heat waves

3.1.1 Mean near-surface air temperature

Figure 4 shows the differences in 2-meter near surface air temperature (T2m) among the three experiments to quantify the UHI and aerosol effects from urbanization (Table 3). The UHI effect causes an increase in near-surface temperature over the urbanized area in summer. The average temperature increase is about 0.53 °C over urban area and 1.49 °C in commercial areas outlined by the green contours (see Fig. 4a). In winter, the UHI warming effect occurs primarily in commercial areas, where the mean temperature increases by about 0.7 °C. In areas surrounding the central commercial region, however, temperature decreases due to the urban land-cover change (shown in Fig. 4d). Such a cooling effect in winter has also been found in previous studies (e. g., Oke, 1982; Jauregui et al., 1992; Wang et al., 2007). The "cool island" effects of urbanization during daytime in winter can be explained by the much larger surface thermal inertia of urban areas than that of rural areas with very low vegetation cover during winter (Wang et al., 2007). Although the wintertime cooling effect in urbanized area is not widely recognized, it is an important phenomenon that is also simulated by the model.

The increased aerosols induced by urbanization exert a cooling effect over the entire simulation domain in both summer and winter (Fig. 4b and 4e). On a domain average, the temperature reduction induced by increased aerosols is less than the warming induced by the UHI effect in both seasons. Therefore, the net urbanization impact (including both land-cover change and aerosol increase) on near-surface temperature is dominated by the UHI warming effect (Fig. 4c and 4f) resulted from the land-cover change in the YRD.

3.1.2 Surface solar radiation

The effects of urban land-cover change and increased aerosols on surface net shortwave radiation are shown in Fig. 5. As the building clusters reduce surface albedo (Oke, 1987), land-cover change increases the net shortwave radiation over urbanized areas, with an average increase of 9.11 W m^{-2} in summer and 8.49 W m^{-2} in winter. The net increase is greater in summer than in winter because of the stronger summertime incoming solar radiation. On the contrary, aerosols reduce the surface net shortwave radiation in the northern part of the domain corresponding to the larger SO_2 and BC emission rates (Fig. 1), with a magnitude of 8.79 W m^{-2} in summer and 7.63 W m^{-2} in winter. Different from the UHI effect that is more localized, the radiative impact of aerosols is more widespread and significant west of the major urban areas and even over the ocean. Figure 6 shows the spatial pattern of mean surface winds simulated in LU70E70 and the difference in column-integrated PM2.5 mass concentration between LU70E06 and LU70E70. Consistent with the prevailing monsoon circulation, southeasterly (northeasterly) flows dominate the YRD in summer (winter), which lead to increases in the PM2.5 concentration over the downwind area of the YRD city clusters. The increased PM2.5 concentrations downwind of the YRD reduce solar radiation to the west (southwest) of the YRD in summer (winter), as shown in Figs. 5b and 5d. Hence aerosol effects on radiation are not limited to the emission source areas in metropolitan regions.

3.1.3 Heat waves

The UHI effect can significantly increase the near-surface temperatures in summer, thereby exacerbating extreme heat waves in urbanized areas (Stone, 2012). By definition, a heat wave occurs when the near-surface temperature reaches or exceeds 35 °C for three or more consecutive

256   days (Tan et al., 2004). The averaged heat wave days comparing LU06E06 and LU70E06 increase

257   at a rate of 3.7 d/yr in the major mega cities (Fig. 7a). The increase is most pronounced in Shanghai,

258   with a rate larger than 12 d/yr.

259   High temperature during heat wave contributes to heat exhaustion or heat stroke, but the

260   impact of atmospheric humidity on evaporation is also crucial. Here we use a heat stress index to

261   assess the combined effects of temperature and humidity on human health due to the UHI effect,

262   expressed as (Masterson and Richardson, 1979):

263    $$Humidex = Ta + (5/9)(e - 10) \qquad (1)$$

264   where Ta is near-surface air temperature (°C) and e is water vapor pressure (hPa). Figure 7b depicts

265   a big increase in heat stress index (Humidex) over urbanized regions in the YRD, except for the

266   city of Hangzhou. The increase in heat stress index is more accentuated in Shanghai, with a mean

267   increase of 2.16, relative to other urban areas. This suggests that humidity has a larger influence

268   on heat stress in Shanghai because of its proximity to the ocean compared to urban areas further

269   inland. In contrast, increased aerosols have little impact on heat waves (results not shown) because

270   their impacts on near-surface temperature are much weaker (Fig. 4b).

271   **3.2 Urbanization effects on summertime precipitation**

272   **3.2.1 Long-term impact on extreme rainfall**

273   Previous studies have provided evidence of urbanization effect on precipitation distribution

274   in and around urban areas (e.g. Shepherd et al., 2003; Kaufmann et al., 2007; Miao et al., 2010).

275   Several mechanisms have been proposed for the effects of urbanization on precipitation: (1) the

276   UHI effect can destabilize the planetary boundary layer (PBL) and trigger convection; (2)

277 increased surface roughness may enhance atmospheric convergence that favors updrafts; (3)

278 building obstruction tends to bifurcate rainfall systems and delays its propagation; (4) the change

279 in land-cover decreases local evaporation, (5) anthropogenic emissions increase aerosol loading in

280 the atmosphere, with subsequent effects on precipitation through changes in radiation and cloud

281 processes. These mechanisms contribute to positive and negative changes in precipitation, leading

282 to more complicated effects on precipitation than temperature.

283 In this section we analyze the results of the three 5-year simulations to examine the long-

284 term impact of urbanization on precipitation. The results show that influences of both urban land

285 cover and elevated aerosols on annual and seasonal mean precipitation are relatively small (not

286 shown). This may be due to the urbanization effect for different rainfall events offsetting each

287 other, leading to an overall weak effect on a longer time scale (see Section 3.2.2). Here we focus

288 on the frequency of extreme rainfall over the YRD region. Extreme summer rainfall events are

289 defined using hourly precipitation rate that is above 95th percentile at each grid for the period of

290 2006-2010. Figure 8 shows the diurnal cycles of extreme rainfall frequency and urbanization-

291 induced changes in the areas around Nanjing, Shanghai, and Su-Xi-Chang (shown in Fig. 1b). The

292 frequency of hourly extreme rainfall reaches its maximum at around 16:00-17:00 LST over three

293 urban clusters. Urban land-cover change increases the occurrence of extreme precipitation in the

294 afternoon (12:00 to 20:00 LST). The maximum increase in the frequency of extreme hourly rainfall

295 events for Nanjing, Shanghai, and Su-Xi-Chang can reach 0.86%, 1.09%, and 0.79%, respectively,

296 with the peak increase occurring in the late afternoon. On the contrary, aerosols exert an opposite

297 impact to substantially reduce the frequency of extreme rainfall in the afternoon by up to 1.05%,

298 0.75%, and 0.72% for Nanjing, Shanghai, and Su-Xi-Chang, respectively. These impacts are

299 significant compared to the maximum frequency of hourly extreme rainfall of about 10% in each

300   area. However, opposite effects of land-cover and aerosol emission changes result in a small net

301   urbanization effect on extreme precipitation.

302   Because urbanization influences extreme precipitation primarily in the afternoon, we further

303   analyze extreme rainfall events with a focus on the averages from 1200 to 2000 LST. Figure 9

304   shows the substantial increase in extreme precipitation frequency concentrated over the major

305   metropolitan areas in the YRD, with some compensation in the surrounding areas in general.

306   Aerosols, however, reduce the occurrence of extreme precipitation more uniformly in most areas

307   of the domain. The most significant influence of aerosols is found in the northwest part of the

308   domain where aerosol concentrations increase the most downwind of the urban centers (Fig. 6a).

309   Similar to the effects on surface temperature and solar radiation (Figs. 4 and 5), aerosols have a

310   substantial impact on the occurrence of extreme precipitation over a wider area than the effects of

311   urban land-use change.

312   How do changes in land cover and aerosols modulate extreme rainfall frequency? Figure 10a

313   shows the diurnal time-height cross section of the impact of urban land-cover (i.e., the difference

314   between LU06E06 and LU70E06) on temperature and divergence averaged over the three city

315   clusters (Nanjing, Shanghai, and Su-Xi-Chang). Air temperature over the urbanized areas increases

316   significantly in the afternoon (from 1200 to 1800 LST) due to the UHI effect. The warming and

317   the increased roughness length in urban areas favor convergence in the lower atmosphere and

318   divergence above. As a result, the mean updraft increases over the urbanized areas in the afternoon

319   (Fig. 10b), which increases cloud water from the lower to middle troposphere in the afternoon.

320   Shortly before noon, there is a small reduction in low clouds, which may be related to the reduced

321   relative humidity due to warmer temperature and/or reduced evaporation from the urban land

322   cover, the so-called urban dry island effect (e.g., Hage, 1975; Wang and Gong, 2009). The increase

323   in cloud water in the afternoon is consistent with the enhanced updrafts. This mechanism

324   potentially explains the increased frequency of extreme precipitation in urban areas in the

325   afternoon (e.g. Craig and Bornstein, 2002; Rozoff et al., 2003; Wan et al., 2013; Zhong and Yang,

326   2015a, 2015b).

327   To understand the aerosol-induced reduction in extreme rainfall events, we analyze the

328   diurnal cycle of aerosol effect (i.e., the difference LU70E06 and LU70E70) on radiative heating,

329   vertical velocity, and net solar radiation at the surface (Fig. 11). As BC emission rates are relatively

330   high in the YRD region (Fig. 2d), aerosols heat the atmosphere due to absorption of solar radiation

331   during daytime (from 08:00 to 17:00 LST). As a result of absorption and scattering of solar

332   radiation by aerosols, less solar radiation reaches the surface. These changes at the surface and in

333   the atmosphere stabilize the atmosphere and reduce convective intensity in the afternoon (from

334   14:00 to 20:00 LST), which reduces the frequency of extreme rainfall events (Koren et al., 2004;

335   Qian et al., 2006; Zhao et al., 2006; 2011; Fan et al., 2007). Although aerosols can enhance

336   precipitation through cloud microphysical changes that invigorate convection (e.g., Khain et al.,

337   2009; Rosenfeld et al., 2008; Fan et al., 2013), aerosol radiative effects generally dominate in

338   China because of the high AOD and strong light-absorbing aerosol properties (Yang et al., 2011;

339   Fan et al., 2015).

340   **3.2.2 Synoptic influence on urbanization impacts**

341   The impacts of urbanization-induced UHI and aerosols on precipitation may be highly

342   variable under different synoptic conditions that influence the atmospheric circulation and cloud

343   and boundary layer processes. Precipitation changes due to urbanization effects may offset each

344   other under different synoptic conditions, leading to an overall weak effect on mean precipitation

345   at longer time scales as discussed in section 3.2.1. We select two typical heavy late-afternoon

346   rainfall events with different background circulations over the YRD region. Case A occurred from

347   08:00 LST 23 June to 08:00 LST 24 June 2006 and case B occurred from 08:00 LST 1 July to

348   08:00 LST 2 July 2006. Figure 12a and 12d show the mean precipitation rate and 850 hPa winds

349   for case A and case B, respectively. Southwesterly flow dominates the entire region in case A (Fig.

350   12a), while in case B (Fig. 12d) southwesterly and northwesterly winds dominate the southern and

351   northern parts of precipitation area, respectively. The averaged background wind speed in case B

352   is much stronger than that in case A, representing stronger synoptic forcing in case B. The effects

353   of urban land-cover change and aerosols on precipitation for the case A (case B) are illustrated in

354   Figs. 12b and 12c (Figs. 12e and 12f), respectively. Both cases show significant precipitation

355   responses to the forcing of urban land-cover and aerosols. We can see that urban land cover

356   increases the rainfall intensity in case A but aerosols decrease precipitation over the urbanized area

357   (Figs. 12b and 12c). The precipitation response to urban land cover and aerosols is just the opposite

358   in case B (Figs. 12e and 12f). Figs. 13a and 13d illustrate the evolution of precipitation in region

359   R1 (Fig. 12a) and R2 (Fig. 12d), respectively, for the two cases. In both cases, rainfall mainly

360   occurred between 08:00 LST and 20:00 LST. The corresponding impacts of urban land-cover and

361   aerosols are shown in Figs. 13b-c and Figs. 13e-f for cases A and B, respectively. In case A, the

362   urban land-cover substantially increases the precipitation intensity in the afternoon with a

363   maximum increase of 6.87 mm h^{-1}. Aerosol effects, on the contrary, decrease the rainfall intensity

364   with a maximum reduction of 3.85 mm h^{-1}. In case B, however, effects of urban land-cover and

365   enhanced aerosols on precipitation are opposite to that in case A. A maximum rainfall reduction of

366   3.81 mm h^{-1} is found to be associated with the effect of urban land cover and an increase of 2.85

367   mm h^{-1} is associated with the aerosol forcing.

368   Why do urban land-cover and aerosols exert opposite effects on precipitation during the

369   two rainfall events? Here we attempt to answer this question by examining the dynamical and

370   thermodynamical changes induced by the UHI and aerosols using the moisture flux convergence

371   (MFC), which is defined as:

372    $$\text{MFC} = -\nabla \cdot \left(q \overrightarrow{V_h} \right) = -q \nabla \cdot \overrightarrow{V_h} - \overrightarrow{V_h} \cdot \nabla q \qquad (2)$$

373   The first and second terms on the right hand side of Eq. 2 denote wind convergence (CON) and

374   moisture advection (MA), respectively.

375   Figures 14a and 14b illustrate the time-height cross sections of changes in moisture flux

376   convergence and cloud water mixing ratio induced by land-cover and aerosol changes over the

377   region R1 (Fig. 12a) during the rainy period in case A. Urban land-cover enhances the convergence

378   of moisture fluxes in the lower troposphere, which results in increased precipitation (Fig. 14a). On

379   the contrary, aerosols weaken the convergence of moisture fluxes and thus reduce precipitation

380   (Fig. 14b). These changes are consistent with those associated with extreme rainfall changes shown

381   in Fig. 10. Interestingly for case B over R2, urban land-cover weakens the convergence of moisture

382   fluxes (Fig. 14c) and thus suppresses precipitation (Fig. 13e) from 08:00 LST 1 July to 02:00 LST

383   2 July 2006. Aerosols, however, enhance the convergence of moisture fluxes over R2 (Fig. 14d)

384   and thus increase precipitation (Fig. 13f). These results establish obvious correspondence between

385   moisture flux convergence changes and the precipitation response to urban land cover and aerosols

386   in the two rainfall events and suggest different processes may dominate the moisture flux

387   convergence changes for the two cases.

388   Figure 15 presents the time-height cross section of the changes in the two terms of MFC,

389   i.e., CON (convergence) and MA (moisture advection), induced by land-cover and aerosol changes

390   averaged over R1 (Fig. 12a) for case A and over R2 (Fig. 12d) for case B. Urban land-cover

391   enhances the wind convergence over R1 in case A (Fig. 15a), leading to an increase in CON by up

392   to 1.56×10^{-4}g kg^{-1} s^{-1}, which is much larger than the increase of 0.61×10^{-4} g kg^{-1} s^{-1} averaged over

393   R2 (Fig. 15c) in case B. The larger enhancement of convergence in case A is attributed to the strong

394   UHI-induced surface heating during this rainfall period (figure not shown). In contrast, aerosols

395   reduce the convergence in both case A and case B due to the aerosol cooling effect near the surface,

396   as discussed previously (Fig. 11). The reduction of convergence in case A is more significant than

397   that in case B because of the larger aerosol loading and, therefore, stronger surface cooling over

398   R1 in case A (not shown). Urban land-cover reduces moisture advection in both cases, with a

399   maximum decrease of -0.99 and -1.89 10^{-4}g kg^{-1} s^{-1}, respectively. Aerosols, however, increase

400   moisture advection, and the maximum increases are 0.93 and 1.31 10^{-4}g kg^{-1} s^{-1} in case A and case

401   B, respectively. Our results show clearly that the changes in CON are opposite to that in MA. As

402   the impacts of urban land-cover and aerosols on moisture advection are greater in case B than in

403   case A, the net changes in the moisture flux convergence are dominated by MA in case B and by

404   CON in case A, leading to opposite effects between the two cases.

405   The significant differences in the responses of MA between the two cases are related to

406   different background circulations during the two events (Figs. 12a and 12d). Weaker southwesterly

407   flow dominates the entire region in case A (Fig. 12a), while in case B (Fig. 12d) stronger

408   southwesterly and northwesterly winds dominate the southern and northern parts of precipitation

409   area, respectively. The changes in MA could be further decomposed into three terms, as shown

410   below in Eq. 3:

411
$$-\Delta V \cdot \nabla q = -V_{ctrl} \cdot \Delta(\nabla q) - (\nabla q)_{ctrl} \cdot \Delta V - \Delta(\nabla q) \cdot \Delta V \qquad (3)$$

412   The first term on the right-hand side of is associated with the change in water vapor, while

413   the second term is associated with the change in circulation. The third term is a nonlinear term

414   including the contribution of both the moisture and circulation changes. Figure 16 illustrates the

415   changes in the first and second term, respectively. The contribution of the third nonlinear term is

416   small and negligible compared to the other two terms (not shown). Urban land-cover reduces the

417   first term in both cases, with a maximum decrease of -0.34 and -1.54 10^{-4}g kg^{-1} s^{-1}, respectively.

418   Aerosols, however, increase the first term, and the maximum increases are 0.49 and 1.78 10^{-4}g kg^{-}

419   ^{1} s^{-1} in case A and case B, respectively. The urban land-cover and aerosol effects on the second

420   term are quite similar for both cases. Therefore, the most significant difference between these two

421   cases is the change in the first term, which is directly associated with the background circulation.

422   These changes in the first term are much larger in case B because of the stronger background winds

423   than in case A, contributing to a more significant modification in MA as shown in Figure 15.

424   In summary, case B represents stronger synoptic forcing than case A. The stronger winds

425   and larger spatial coverage of clouds and precipitation associated with the larger scale synoptic

426   system weakens the UHI and aerosol effects through ventilation and changes in radiation, resulting

427   in weaker CON and larger MA changes. Conversely, with weaker synoptic forcing, the stronger

428   UHI and aerosol effects enhance the changes in CON while MA effects are smaller due to the

429   weaker background winds. Therefore, our results highlight the distinguishing role of synoptic

430   forcing on how urban land-cover and aerosol influence the dynamical and thermo-dynamical

431   environments and precipitation.

432   **4. Summary**

433   In this study, the state-of-the-art WRF-Chem model coupled with a single-layer UCM, is run

434   at convection-permitting scale to investigate the influences of urbanization-induced land-cover

435   change and elevated aerosol concentrations on local and regional climate in the Yangtze River

436   Delta (YRD) in China. A 5-year period (2006-2010) is selected for multi-year simulations to

437   investigate urbanization effects on extreme events and the role of synoptic forcing. Three

438   experiments were conducted with different configurations of land cover and aerosol emissions: (1)

439   urban land and emissions in 2006, (2) urban land in the 1970s and emissions in 2006, and (3) urban

440   land and emissions in the 1970s. The experiment with the 2006 land-use type and anthropogenic

441   emissions reproduces the observed spatial patterns of near-surface air temperature and

442   precipitation fairly well.

443   The expanded urban land cover and increased aerosols have opposite impacts on the near-

444   surface air temperature. The urban land-use change increases 2-m air temperature due to the UHI

445   effect in commercial areas with a domain-averaged increase of 1.49 °C in summer and 0.7 °C in

446   winter. In the surrounding areas, however, surface air temperature increases in summer but

447   decreases in winter. The latter is attributed to the much greater thermal initial over urban areas

448   than over rural areas in wintertime when both vegetation cover and soil moisture are at their

449   seasonal minimum. Compared to the effect of land-cover change, aerosol effect exerts a less

450   significant influence on near-surface temperature with minor decreases in both summer and winter.

451   Overall, the impact of urban land-use change outweighs that of enhanced aerosols on regional

452   temperature especially in summer. The increase in near-surface temperature induced by the UHI

453   effect leads to an increase in heat wave days by 3.7 days per year over the major mega cities in the

454   YRD region. The greater response of solar radiation to urban land-cover in summer is the major

455   factor contributing to the larger changes in surface temperature in summer than in winter.

456 Compared to the urban land-use effect, aerosol effect on reducing the surface solar radiation occurs

457 over a much broader region including the downwind area of the city clusters.

458 The urban land-cover change and increased aerosols have opposite effects on the frequency

459 of extreme rainfall during summer. The UHI effect leads to more frequent extreme precipitation

460 over the urbanized area in the afternoon because of an enhanced near-surface convergence and

461 vertical motion. In contrast, aerosol tends to decrease the frequency of extreme precipitation

462 because of its cooling effect near the surface and heating effect (by light-absorbing particles)

463 above, leading to an increased atmospheric stability and weakened updrafts. Additional aerosols

464 can also induce decreases in the frequency of extreme precipitation over non-urban areas,

465 particularly in the downwind area of the city clusters.

466 The effects of both urban land-cover and increased aerosols on summertime rainfall vary

467 with synoptic weather systems and environmental conditions. Two late-afternoon rainfall events

468 are selected for in-depth analysis. For the two cases, urbanization exerts similar impacts on local-

469 scale convergence and mean wind speed, which modify the strength of moisture transport. More

470 specifically, the effect of urban land-cover increases local-scale convergence due to the UHI-

471 induced circulation and reduces low-level wind speed, while aerosols have an opposite effect due

472 to the cooling near the surface. We found that the impacts of urban land-cover and aerosol on

473 precipitation are determined not only by their effect on local-scale convergence, but also

474 modulated by the large-scale weather systems. Our analyses suggest that synoptic forcing plays a

475 significant role in how urbanization-induced land-cover and aerosols influence individual rainfall

476 event. Although the two rainfall events selected for the analysis do not represent all types of

477 precipitation events in the YRD Region, they demonstrate how the effect of urbanization on

478 precipitation may vary and offset each other under different synoptic conditions, leading to an

479 overall weak effect on mean precipitation at longer time scales. To further quantify urbanization

480 effects, uncertainties in anthropogenic emissions and heating, unresolved urban building and

481 streets structure, and representation in aerosol-cloud interactions and cloud microphysics in the

482 model should be investigated in future studies. Further investigation is also needed to have a better

483 and more comprehensive understanding of the complicated mechanisms through which

484 urbanization influences heavy rainfall under a full range of weather conditions.

485
Acknowledgments

487   The contributions of PNNL authors are supported by the U.S. Department of Energy's

488 Office of Science as part of the Regional and Global Climate Modeling Program and Atmospheric

489 System Research (ASR) program. The contribution of Shi Zhong and Xiu-Qun Yang is supported

490 by the National Basic Research Program of China (2010CB428504), Jiangsu Collaborative

491 Innovation Center for Climate Change, and the Scholarship Award for Excellent Doctoral Student

492 granted by China Scholarship Council. The work of Ben Yang is supported by the National Natural

493 Science Foundation of China (41305084). Computations were performed using resources of the

494 National Energy Research Scientific Computing Center (NERSC) at Lawrence Berkeley National

495 Laboratory and PNNL Institutional Computing. The Pacific Northwest National Laboratory is

496 operated for DOE by Battelle Memorial Institute under contract DE-AC05-76RL01830. All model

497 results are archived on a PNNL cluster and available upon request. Please contact Yun Qian

498 (yun.qian@pnnl.gov).

499

500

501

502

503

504

Reference

Baik, J. J., Kim, Y. H., Kim, J. J., and Han, J. Y.: Effect of boundary-layer stability on urban heat island induced circulation, Theor. Appl. Climatol., 89, 73–81, 2007.

Bauer, S. E., and Menon, S.: Aerosol direct, indirect, semidirect, and surface albedo effects from sector contributions based on the IPCC AR5 emissions for preindustrial and present-day conditions, J. Geophys. Res., 117, D01206, doi: 10.1029/2011JD016816, 2012.

Bornstein, R., and Lin, Q.: Urban heat islands and summertime convective thunderstorms in Atlanta: Three cases studies, Atmos. Environ., 34, 507–516, 2000.

Braham, R. R.: Comments on "Urban, topographic and diurnal effects on rainfall in the St. Louis region". J. Appl. Meteorol., 18, 371-374, 1979.

Changnon, S. R.: Rainfall changes in summer caused by St. Louis, Science, 205, 402–404, 1979.

Charlson, R. J., et al.: Climate forcing by anthropogenic aerosols, Science, 255, 423–430, 1992.

Che, H. Z., Shi, G. Y., Zhang, X. Y., Arimoto, R., Zhao, J. Q., Xu, L., Wang, B., and Chen, Z. H.: Analysis of 40 years of solar radiation data from China, 1961–2000, Geophys. Res. Lett., 32, L06803, doi:10.1029/2004GL022322, 2005.

Chen, F., Kusaka, H., Bornstein, R., et al.: The integrated WRF/urban modeling system: development, evaluation, and applications to urban environmental problems, Int. J. Climatol., 31(2), 273-288, 2001.

Coakley, J. A., Bernstein, R. L., and Durkee, P. A.: Effect of ship-track effluents on cloud reflectivity, Science, 273, 1020–1022,1987.

Craig, K., and Bornstein, R.: MM5 simulation of urban induced convective precipitation over Atlanta. Preprints, Fourth Conf. on the Urban Environment, Norfolk, VA, Amer. Meteor. Soc., 5–6, 2002.

Dentener, F., et al.: Emissions of primary aerosol and precursor gases in the years 2000 and 1750 prescribed data-sets for AeroCom, Atmos. Chem. Phys., 6, 4321–4344, doi:10.5194/acp-6-4321-2006, 2006.

Du, Y., et al.: Impact of urban expansion on regional temperature change in the Yangtze River Delta, J. of Geophys. Sci., 17(4): 387-398, 2006.

Fast, J. D, et al.: Evolution of ozone, particulates, and aerosol direct forcing in an urban area using a new fully-coupled meteorology, chemistry, and aerosol model, J. Geophys. Res., 111, D21305, doi:10.1029/2005JD006721, 2006.

Fan, J., Leung, L. R., Rosenfeld, D., Chen, Q., Li, Z., Zhang, J., and Yan, H.: Microphysical Effects Determine Macrophysical Response for Aerosol Impacts on Deep Convective Clouds, Proceedings of the National Academy of Sciences of the United States of America, 110(48), E4581-E4590, doi:10.1073/pnas.1316830110, 2013.

Fan, J., Rosenfeld, D., Yang, Y., Zhao, C., Leung, Y. R., and Li, Z.: Substantial Contribution of Anthropogenic Air Pollution to Catastrophic Floods in Southwest China, Geophys. Res. Lett., 42(14), 6066-6075, doi:10.1002/2015GL064479, 2015.

Fan, J., Zhang, R., Li, G., Tao, W., and Li, X.: Simulations of cumulus clouds using a spectral microphysics cloud resolving model, J. Geophys. Res., 112, D04201, doi:10.1175/2010JAS3651.1, 2007.

546 Feingold G., Koren, I., Wang, H., Xue, H., and Brewer W.: Precipitation-generated oscillations in

547   open cellular cloud fields. *Nature, 466*, 849–852, 2010.

548 Grell, G. A., Peckham, S. E., Schmitz, R., et al.: Fully coupled ''online'' chemistry within the WRF

549   model, Atmos. Environ., 39, 6957–6975, 2005.

550 Gustafson, W. I., Chapman, E. G., Ghan, S. J., Easter, R. C., and Fast, J. D.: Impact on modeled

551   cloud characteristics due to simplified treatment of uniform cloud condensation nuclei during

552   NEAQS 2004, Geophys. Res. Lett., 34, L19809 doi:10.1029/2007GL0300321,2007.

553 Guo, X., Fu, D., and Wang, J.: Mesoscale convective precipitation system modified by

554   urbanization in Beijing city, Atmos. Res., 82, 112–126, 2006.

555 Hage, K. D.: Urban-rural humidity difference, J. Appl. Meteor., 14(7), 1277-1283, 1975.

556 Hansen, J., Sato, M., and Ruedy, R.: Radiative Forcing and Climate Response, J. Geophys. Res.,

557   102, 6831–6864, 1997.

558 Hjemfelt, M. R.: Numerical simulation of the effects of St. Louis on mesoscale boundary layer

559   airflow and vertical motion: Simulations of urban vs. non-urban effects, J. Appl. Meteor., 21,

560   1239–1257, 1982.

561 Hu, Y., Ban, Y., Zhang., Q., and Liu, J.: The trajectory of urbanization process in the Yangtze River

562   Delta during 1990 to 2005. 7th Urban Remote Sensing Joint Event, 20–22 May 2009,

563   Shanghai, DOI: 10.1109/URS.2009.5137536, 2009.

564 Huff, F. A., and Changnon Jr., S. A.: Climatological assessment of urban effects on precipitation

565   at St. Louis, J. Appl. Meteorol., 11, 823-842, 1972.

566 Inoue, T., and Kimura, F.: Urban effects on low-level clouds around the Tokyo metropolitan area

567   on clear summer days, Geophys. Res. Lett., 31, L05103, doi:10.1029/2003GL018908, 2004.

568 Jauregui, E., Godinez, L., and Cruz, F.: Aspects of Heat-Island Development in Guadalajara,

569   Mexico, Atmos. Environ. 26B, 391–396, 1992.

570 Jiang Y, Liu, X., Yang, X. Q.: A numerical study of the effect of different aerosol types on East

571   Asian summer clouds and precipitation, Atmos. Environ., 70, 51-63, 2013.

572 Kaufmann, R. K., Seto, K. C., Schneider, A., Liu, Z., Zhou, L., Wang, W.: Climate response to

573   rapid urban growth: evidence of a human-induced precipitation deficit, J. Climate, 20(10),

574   2299-2306, 2007.

575 Khain A. P.: Notes on state-of-the-art investigations of aerosol effects on precipitation: a critical

576   review, Environ. Res. Lett., 4(1), 015004, 2009.

577 Koren, I., et al.: Measurement of the effect of Amazon smoke on inhibition of cloud formation,

578 Science, 303(5662), 1342-1345, 2004.

579 Kusaka, H., Kikegawa, Y., and Kimura, F.: A simple single layer urban canopy model for

580   atmospheric models: comparison with multi-layer and slab models, Bound-Layer Meteor.,

581   101, 329–358, 2001.

582 Landsberg, H. E.: The Urban Climate, Academic Press, Londen, UK, 1981.

583 Lei, M., et al.: Effect of explicit urban land surface representation on the simulation of the 26 July

584   2005 heavy rain event over Mumbai, India, Atmos. Chem. Phys., 8 (20), 5975-5995, 2008.

585 Lu, Z., Zhang, Q., and Streets, D. G.: Sulfur dioxide and primary carbonaceous aerosol emissions

586 in China and India, 1996–2010, Atmos. Chem. Phys., 11(18), 9839-9864, 2011.

587 Masterson, J., Richardson F. A.: Humidex. A method of quantifying human discomfort due to

588 excessive heat and humidity, Environment Canada, Downsview, 1979.

589 McFarquhar, G. M., and H. Wang: Effects of aerosols on trade wind cumuli over the Indian Ocean:

590 Model simulations, Q. J. R. Meteorol. Soc., 132, 821–843, 2006.

591 Miao, S. G., Chen, F., Li, Q. C., and Fan, S. Y.: Impacts of urban processes and urbanization on

592 summer precipitation: a case study of heavy rainfall in Beijing on 1 August 2006, J. Appl.

593 Meteorol. Climatol., 50, 806–825, 2010.

594 Monin, A. S., and Obukhov, A. M.: Basic laws of turbulent mixing in the surface layer of the

595 atmosphere, Contributions of the Geophysical Institute of the Slovak Academy of Sciences,

596 24, 151, 163–187, 1954.

597 Oke, T. R.: The Energetic Basis of the Urban Heat Island, Q. J. R. Met. Soc., 108, 1–22, 1982.

598 Oke, T. R.: Boundary Layer Climates. 2d ed. Methuen Co., 435 pp, 1987.

599 Oleson, K. W., Bonan, G. B., Feddema, J., and Vertensten, M.: An urban parameterization for a

600 global climate model. Part II: Sensitivity to input parameters and the simulated urban heat

601 island in offline simulations, J. Appl. Meteor. Climatol., 47, 1061-1076, 2008.

602 Qian, Y., Kaiser, D. P., Leung, L. R., and Xu, M.: More frequent cloud-free sky and less surface

603 solar radiation in China from 1955 to 2000, Geophys. Res. Lett., 33, L01812,

604 doi:10.1029/2005GL024586, 2006.

605 Qian, Y., Wang, W., Leung, L. R., and Kaiser, D. P.: Variability of solar radiation under cloud-free

606   skies in China: The role of aerosols, Geophys. Res. Lett., 34, L12804,

607   doi:10.1029/2006GL028800, 2007.

608 Qian, Y., Gong, D., Fan, J., Leung. L. R., Bennartz, R., Chen, D., Wang, W.: Heavy pollution

609   suppresses light rain in China: Observations and modeling, J. Geophys. Res., 114, D00K02,

610   doi:10.1029/ 2008JD011575, 2009.

611 Qian, Y., Gustafson Jr, W. I., and Fast, J. D.: An investigation of the sub-grid variability of trace

612   gases and aerosols for global climate modeling, Atmos. Chem. Phys., 10, 6917-6946,

613   doi:10.5194/acp-10-6917-2010, 2010.

614 Qian, Y., Teppei, J., Yasunari, J., et al.: Light-absorbing particles in snow and ice: Measurement

615   and modeling of climatic and hydrological impact. Adv. Atmos. Sci., 32(1), 64–91, doi:

616   10.1007/s00376-014-0010-0, 2015.

617 Ren, G., Zhou, Y., Chu, Z., Zhou, J., Zhang, A., Guo, J., Liu, X.: Urbanization Effects on Observed

618   Surface Air Temperature Trends in North China, J. Climate, 21 (6), 1333-1348, 2008.

619 Rosenfeld, D.: Suppression of rain and snow by urban and industrial air pollution, Science, 287

620   (5459), 1793-1796,2000.

621 Rosenfeld, D., et al.: Flood or drought: How do aerosols affect precipitation? Science, 321, 1309–

622   1313, doi:10.1126/ science.1160606, 2008.

623 Rozoff, C., Cotton, W. R., and Adegoke, J. O.: Simulation of St. Louis, Missouri, land use impacts

624   on thunderstorms, J. Appl. Meteor., 42, 716–738, 2003.

625 Schell, B., Ackermann, I. J., Hass, H., Binkowski, F. S., and Ebel, A.: Modeling the formation of

626   secondary organic aerosol within a comprehensive air quality modeling system, J. Geophys.

627   Res., 106, 28275–28293, 2001.

628 Sen Roy, S., and Yuan, F.: Trends in extreme temperatures in relation to urbanization in the Twin

629   Cities Metropolitan Area, Minnesota. J. Appl. Meteor., 48 (3), 669-679, 2009.

630 Shepherd, J. M., and Burian, S. J.: Detection of urban-induced rainfall anomalies in a major coastal

631   city, Earth Interactions, 7(4), 1-17, 2003.

632 Shepherd, J. M., Carter, M., Manyin, M., Messen, D., and Burian, S.: The impact of urbanization

633   on current and future coastal precipitation: a case study for Houston, Environ. Plan., 37, 284-

634   304, 2010.

635 Shepherd, J. M.: A review of current investigations of urban-induced rainfall and recommendations

636   for the future, Earth Interact., 9 (12), 1-27, 2005.

637 Skamarock, W. C., Klemp, J. B.: A time-split nonhydrostatic atmospheric model for weather

638   research and forecasting applications, J. Computational Physics, 227(7): 3465-3485, 2008.

639 Stone, B.: The city and the coming climate: Climate change in the places we live, Cambridge

640   University Press, New York, 2012.

641 Stockwell, W. R., Middleton, P., Chang, J. S., and Tang, X.: The second generation regional acid

642   deposition model chemicalmechanism for regional air quality modeling, J. Geophys. Res.,

643   95, 16343–16367, 1990.

644 Storer R. L., and Van den Heever, S. C.: Microphysical processes evident in aerosol forcing of

645   tropical deep convective clouds, J. Atmos. Sci., 70(2), 430-446, 2013.

646   Tan J., Kalkstein, L. S., Huang, J., Lin, S., Yin, H., Shao, D.: An operational heat/health warning

647   system in Shanghai, International Journal of Biometeorology, 48(3), 157-162, 2004.

648   Tao, W. K., Chen, J. P., Li, Z., Wang, C., Zhang, C.: Impact of aerosols on convective clouds and

649   precipitation, Rev. Geophys., 50 (2), 2012.

650   Tewari, M., Chen, F., Kusaka, H., and Miao, S.: Coupled WRF/Unified Noah/urban-canopy

651   modeling system, NCAR WRF Documentation. Boulder: NCAR, 1-20, 2007.

652   Wan, H. C., Zhong, Z., Yang, X. Q., and Li, X. Q.: Impact of city belt in Yangtze River Delta in

653   China on a precipitation process in summer: A case study, Atmos. Res., 125-126, 63–75, 2013.

654   Wang, H., and Feingold, G.: Modeling mesoscale cellular structures and drizzle in marine

655   stratocumulus. Part II: The Microphysics and Dynamics of the Boundary Region between

656   Open and Closed Cells, *J. Atmos. Sci., 66*, 3257–3275, 2009.

657   Wang, H., Skamarock, W. C., and Feingold, G.: Evaluation of scalar advection schemes in the

658   Advanced Research WRF model using large-eddy simulations of aerosol–cloud interactions,

659   *Mon. Wea. Rev.*, **137**, 2547–2558, 2009.

660   Wang, X. Q., and Gong, Y. B.: The impact of an urban dry island on the summer heat wave and

661   sultry weather in Beijing City, Chinese Science Bulletin, 55(16), 1657-1661, 2010.

662   Wang, Y., Zhuang, G., Zhang, X., Huang, K., Xu, C., Tang, A., Chen, J., An, Z.: The ion chemistry,

663   seasonal cycle, and sources of PM2.5 and TSP aerosol in Shanghai, Atmos. Environ., 40(16),

664   2935-2952, 2006.

665 Wang, K. C., Wang, J., Wang, P., Sparrow, M., Yang, J., Chen, H.: Influences of urbanization on
666   surface characteristics as derived from the Moderate-Resolution Imaging
667   Spectroradiometer: A case study for the Beijing metropolitan area, J. Geophys. Res., 112.
668   D22S06, 2007.

669 Wang, X. M., Sun, X. G., Tang, J. P., and Yang, X. Q.: Urbanization-induced regional warming in
670   Yangtze River Delta: potential role of anthropogenic heat release, Int. J. Climatol., doi:
671   10.1002/joc.4296, 2015.

672 Wienert, U., and Kuttler, W.: The dependence of the urban heat island intensity on latitude–a
673   statistical approach, Meteorologische Zeitschrift, 14(5), 677-686, 2005.

674 Wu, Kai, and Yang, X. Q.: Urbanization and heterogeneous surface warming in eastern China,
675   Chinese Science Bulletin, 58 (12), 1363-1373, 2013.

676 Yang, Ben, Zhang, Y. C., and Qian, Y.: Simulation of urban climate with high-resolution WRF
677   model: A case study in Nanjing, China, Asia-Pacific J. Atmos. Sci., 48 (3), 227-241, 2012.

678 Yang, X., Hou, Y., Chen, B.: Observed surface warming induced by urbanization in east China, J.
679   Geophys. Res., 116 (D14), 2011.

680 Yu, H., Kaufman, Y. J., Chin, M., et al.: A review of measurement-based assessments of the aerosol
681   direct radiative effect and forcing, Atmos. Chem. Phys., 6 (3), 613-666, 2006.

682 Zhang, N., Gao, Z., Wang, X., Chen, Y.: Modeling the impact of urbanization on the local and
683   regional climate in Yangtze River Delta, China, Theor. Appl. Climatol., 102(3-4): 331-342,
684   2010.

685   Zhang, Q., Hu, Y., Liu, J.: The trajectories of urban land and industrial land in Shanghai over the

686   past 30 years, Urban Remote Sensing Event, 2009 Joint. IEEE , 2009a.

687   Zhang, Q., Streets, D. G., Carmichael, G. R., et al.: Asian emissions in 2006 for the NASA INTEX-

688   B mission, Atmos. Chem. Phys., 9, 5131–5153, doi:10.5194/acp-9-5131-2009, 2009b.

689   Zhao, C., Tie, X., Lin, Y.: A possible positive feedback of reduction of precipitation and increase

690   in aerosols over eastern central China, Geophys. Res. Lett., 33(11), 2006.

691   Zhao, C., Liu, X., Leung, L. R., Johnson, B., MaFarlane, S. A., Gustafson, W. I., Fast, J. D., Easter,

692   R.: The spatial distribution of mineral dust and its shortwave radiative forcing over North

693   Africa: modeling sensitivities to dust emissions and aerosol size treatments, Atmos. Chem.

694   Phys., 11, 1879-1893, 2010.

695   Zhao, C., Liu, X., Leung, L. R., and Hagos, S.: Radiative impact of mineral dust on monsoon

696   precipitation variability over West Africa, Atmos. Chem. Phys., 11, 1879-1893,

697   doi:10.5194/acp-11-1879-2011, 2011.

698   Zhao, C., Leung, L. R., Easter, R., Hand, J., and Avise, J.: Characterization of speciated aerosol

699   direct radiative forcing over California, J. Geophys. Res., 118, 2372–2388,

700   doi:10.1029/2012JD018364, 2013a.

701   Zhao, C., Chen, S., Leung, L. R., Qian, Y., Kok, J., Zaveri, R., and Huang, J.: Uncertainty in

702   modeling dust mass balance and radiative forcing from size parameterization, Atmos.

703   Chem. Phys., 13, 10733–10753, 2013b.

704   Zhong, S., and Yang, X. Q.: Ensemble simulations of the urban effect on a summer rainfall event

705   in the Great Beijing Metropolitan Area, Atmos. Res., 153, 318-334. 2015a.

706   Zhong, S, and Yang, X. Q.: Mechanism of urbanization impact on a summer cold frontal rainfall

707   process in the Great Beijing Metropolitan Area, J. Appl. Meteorol. Climatol., doi:

708   10.1175/JAMC-D-14-0264.1, 2015b.

709   Zhong, S., Qian, Y., Zhao, C., Leung, R., and Yang, X. Q.: A case study of urbanization impact on

710   summer precipitation in the Greater Beijing Metropolitan Area: Urban heat island versus

711   aerosol effects, J. Geophys. Res. Atmos., 120, doi:10.1002/2015JD023753, 2015.

712

713

714

715

716

717

718

Table and Figure Captions

719

720 **Table 1** Configurations of the WRF physics schemes used in the present study.

721 **Table 2** Numerical experiments and corresponding urban land use and aerosol emissions.

722 **Table 3** Analysis strategies for the investigation of urban land-use and/or aerosol effects.

723 **Figure 1** Land-use categories for year (a) 1970; (b) 2006; and (c) SO_2 (units: mol km^{-2} h^{-1}) and (d)

724 black carbon (BC) emission rates (units: ug m^{-2} s^{-1}) averaged over 2006-2010. Surface topography

725 is also shown in Fig. 1a (contour; units: m). The boxes in Fig. 1b outline three mega-city clusters

726 of Nanjing, Su-Xi-Chang, and Shanghai.

727 **Figure 2** Moving spatial anomalies of averaged surface skin temperature (units: °C) with a filtering

728 window size of 1° ×1° for (a) MODIS observation and (b) the L06E06 simulation. The "High

729 Intensity Residential" and "Commercial/Industrial/Transportation" areas are marked with green

730 lines and yellow lines, respectively.

731 **Figure 3** Annual mean (a) near-surface temperature (units: °C) and (b) precipitation (units: mm d^{-}

732 ^{1}) from observations (shaded circles) and the LU06E06 simulation (shaded).

733 **Figure 4** Differences in mean 2-m temperature (Units: °C) between simulations (a, d) LU06E70

734 and LU70E70, (b, e) LU70E06 and LU70E70, (c, f) LU06E06 and LU70E70 for summer (upper

735 panels) and winter (bottom panels). "Commercial/Industrial/Transportation" areas are marked with

736 green lines. The black dots mark the area with statistically significant changes.

737 **Figure 5** Differences in net shortwave fluxes at the surface (units: W m^{-2}) between simulations (a,

738 c) LU06E70 and LU70E70, and (b, d) LU70E06 and LU70E70 in summer (upper panels) and

739 winter (bottom panels).

740 **Figure 6** Differences in column burden of PM2.5 (g m^{-2}) between simulations LU70E06 and

741 LU70E70, superimposed with near-surface winds simulated in LU70E70, for (a) summer and (b)

742 winter.

743 **Figure 7** Differences in mean summertime (a) heat wave days (units: d/yr) and (b) heat stress

744 (units: °C) between simulations LU06E70 and LU70E70.

745 **Figure 8** Diurnal cycles of the frequency of summertime extreme rainfall events for LU70E70

746 (defined using hourly precipitation intensity above 95th percentile, black lines, right axis) and the

747 differences between simulations over (a) Nanjing, (b) Shanghai, and (c) Su-Xi-Chang. Red lines

748 are for Land use effect, blue lines for Aerosol effect, and green lines for the combined effect.

749 **Figure 9** Differences in the frequency of summertime extreme rainfall events (averaged from

750 12:00 to 20:00 LST) between simulations (a) LU06E70 and LU70E70, and (b) LU70E06 and

751 LU70E70.

752 **Figure 10** (a) Time-height cross-sections of differences (between LU06E70 and LU70E70) in

753 temperature (contour; units: °C) and divergence (shade; units: 10^{-5} s^{-1}) averaged over the three city

754 clusters (Nanjing, Shanghai, and Su-Xi-Chang); (b) same as (a), but for vertical velocity (shade;

755 units: 10^{-2} m s^{-1}) and cloud water mixing ratio (contour; 10^{-3} kg kg^{-1}).

756 **Figure 11** Time-height cross-sections of differences between LU70E06 and LU70E70 in radiative

757 heating profile (shade; units: K d^{-1}), vertical velocity (contour; units: 10^{-2} m s^{-1}) and surface solar

758   radiation (blue bars; units: W m^{-2}) averaged over the three city clusters (Nanjing, Shanghai, and

759   Su-Xi-Chang).

760   **Figure 12** Rain rate (units: mm h-1) superimposed with wind vectors at 850 hPa for case A from

761   08:00 LST 23 June to 08:00 LST 24 June 2006 (a) simulated in the LU06E06 simulation, (b)

762   differences between LU06E70 and LU70E70, (c) differences between LU70E06 and LU70E70.

763   Panels (d-f) are the same as (a-c) but for case B from 08:00 LST 1 July to 08:00 LST 2 July 2006**.**

764   The boxes R1 in (a) and R2 in (d) outline the three regions over which further analysis are

765   conducted. Lines across the center of each box mark the cross-sections to be analyzed.

766   **Figure 13** The time evolution of precipitation (units: mm h^{-1}) along the line *ab* (marked in Fig.

767   12a) from 08:00 LST 23 June to 02:00 LST 24 June 2006 (case A) (a) simulated in the LU06E06

768   simulation, (b) differences between LU06E70 and LU70E70, (c) differences between LU70E06

769   and LU70E70. Panels (d-f) are the same as (a-c) but for case B along line *cd* (marked in Fig. 12d)

770   from 08:00 LST 1 July to 02:00 LST 2 July 2006**.**

771   **Figure 14** The time-height cross-sections of differences in moisture flux convergence (shaded;

772   units: 10^{-4} g^{-1} kg^{-1} s^{-1}) and water vapor mixing ratio (black lines; units: 10^{-2} g kg^{-1}) from 08:00 LST

773   23 June to 02:00 LST 24 June 2006 (case A) over region R1 (denoted in Fig. 12a) between (a)

774   LU06E70 and LU70E70; (b) LU70E06 and LU70E70; Panels (c, d) are the same as (a, b) but for

775   case B from 08:00 LST 1 July to 02:00 LST 2 July 2006 over R2 (denoted Fig. 12d).

776   **Figure 15** Same as Fig. 14 but for differences in the CON term (shaded; units: 10^{-4} g^{-1}kg^{-1} s^{-1}) and

777   MA term (black lines; units: 10^{-4} g^{-1} kg^{-1} s^{-1}) in eq. (2).

778   **Figure 16** Same as Fig. 15 but for differences in the first term $(-V_{ctrl} \cdot \Delta(\nabla q))$ (shaded; units: 10^{-4}

779      $g^{-1} kg^{-1} s^{-1}$) and the second term $(- (\nabla q)_{ctrl} \cdot \Delta V)$ (black lines; units: $10^{-4} g^{-1} kg^{-1} s^{-1}$) in Eq.3.

Table 1 Configurations of the WRF physics schemes used in the present study.

Physical processes	Parameterization Scheme
Microphysics	Morrison 2-moment scheme (Morrison et al., 2009)
Long-wave radiation	RRTMG scheme (Iacono et al., 2008)
Short-wave radiation	RRTMG scheme
Surface layer	Monin-Obukhov scheme (Monin and Obukhov, 1954)
Land surface process	Noah land-surface model (Chen et al., 1996; Chen and Dudhia, 2001)
Planetary boundary layer process	Mellor-Yamada-Jajic TKE scheme (Mellor and Yamada, 1982; Janijic, 2001)

Table 2 Numerical experiments and corresponding urban land use and aerosol emissions.

Experiment	Land-use category	Anthropogenic emissions
LU06E06	2006	2006
LU70E06	1970	2006
LU70E70	1970	1970

Table 3 Analysis strategies for the investigation of urban land-use and/or aerosol effects.

Difference	Mechanism
LU06E06- LU70E06	Urban
LU70E06- LU70E70	Aerosol
LU06E06- LU70E70	Urban and aerosol
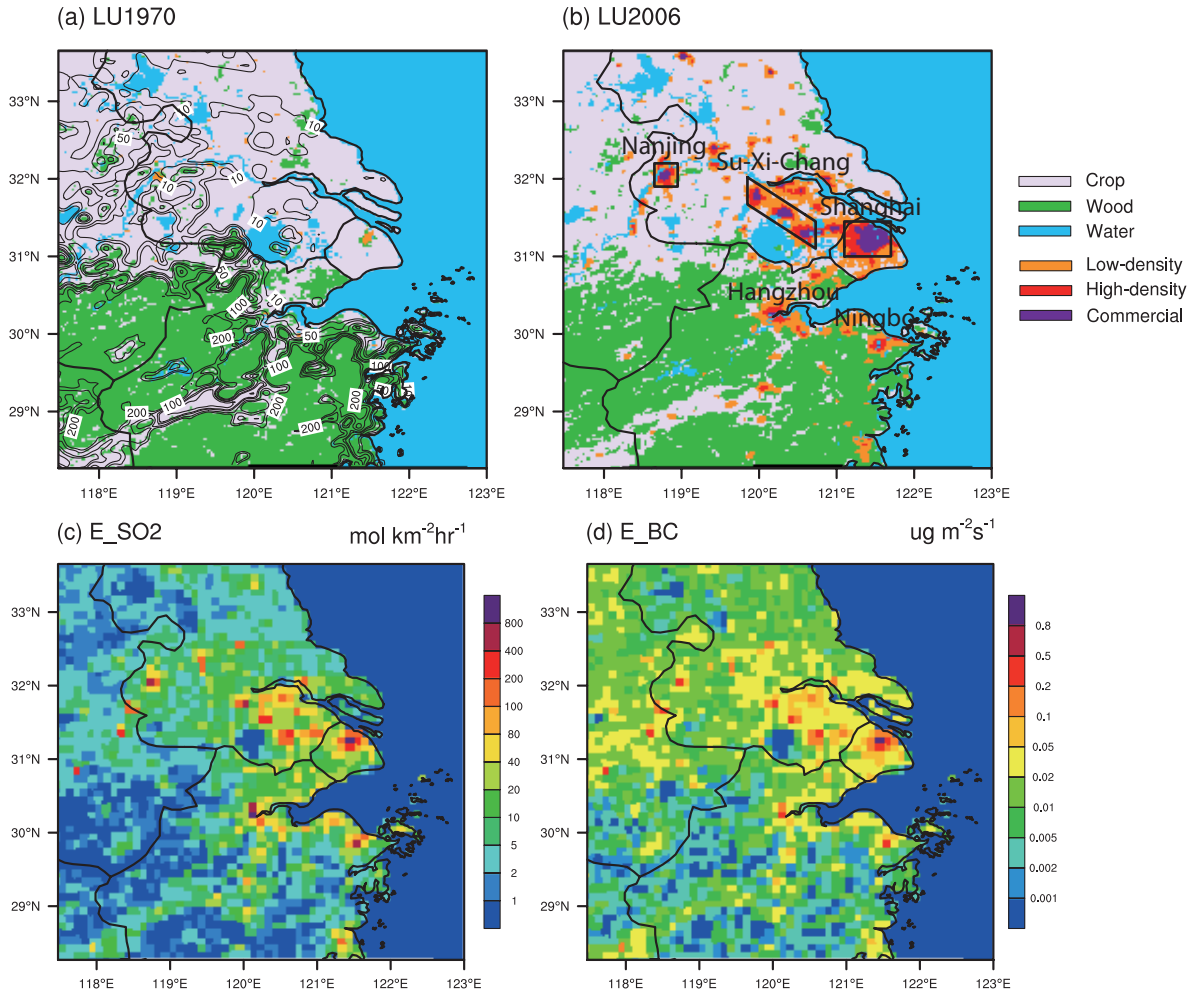
Figure 1 Land-use categories for year (a) 1970; (b) 2006; and (c) SO₂ (units: mol km⁻² h⁻¹) and (d) black carbon (BC) emission rates (units: ug m⁻² s⁻¹) averaged over 2006-2010. The topography is also shown in Fig. 1a (contour; units: m). The boxes in Fig. 1b outline three mega-city clusters of Nanjing, Su-Xi-Chang, and Shanghai.
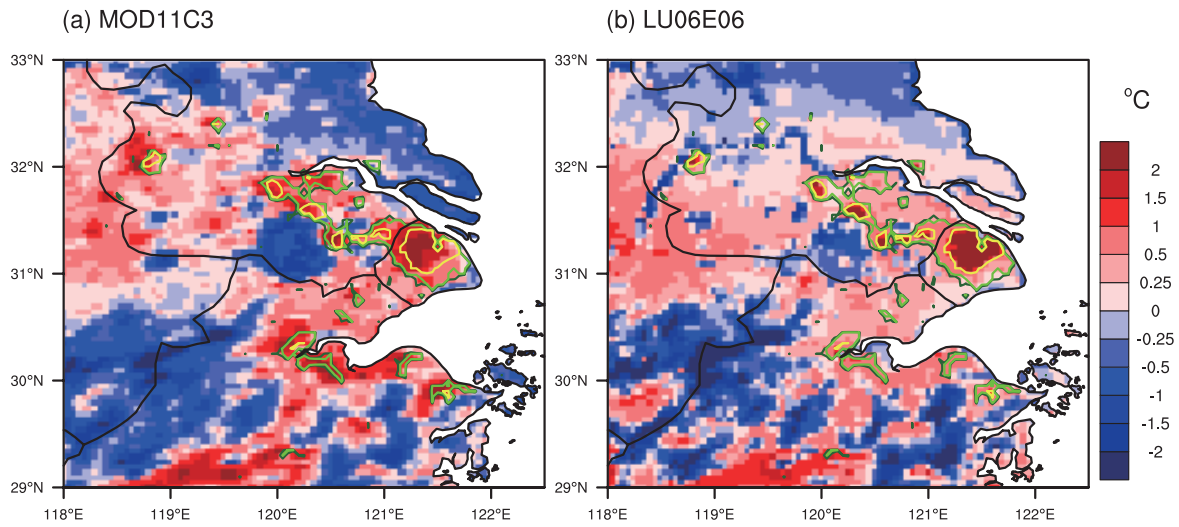
Figure 2 Moving spatial anomalies of averaged surface skin temperature (units: °C) with a filtering window size of 1° ×1° for (a) MODIS observation and (b) the L06E06 simulation. The "High Intensity Residential" and "Commercial/Industrial/Transportation" areas are marked with green lines and yellow lines, respectively.
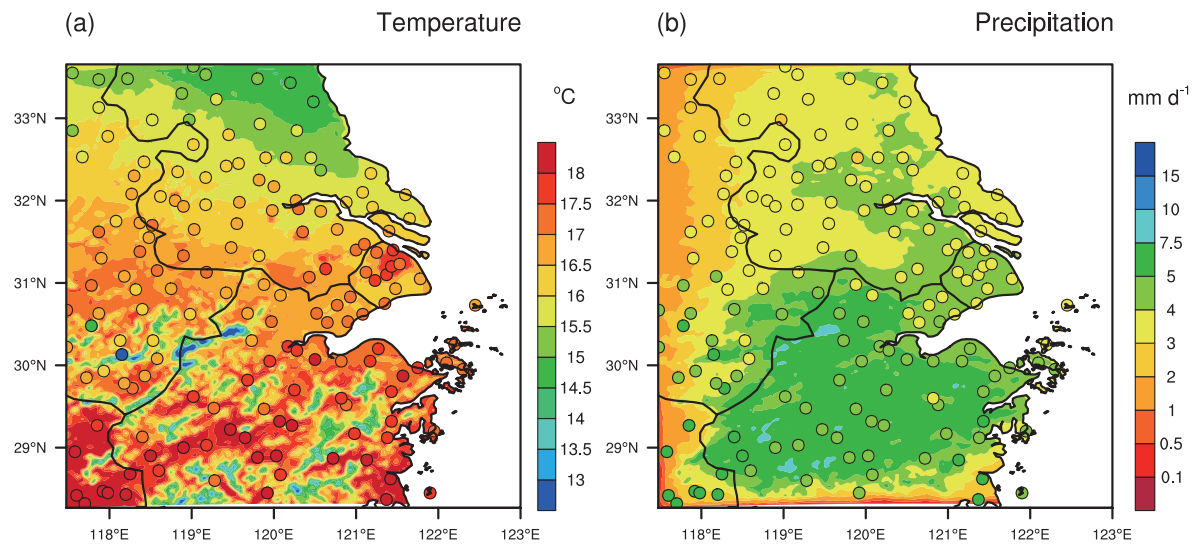
Figure 3 Annual mean (a) near-surface temperature (units: °C) and (b) precipitation (units: mm d^{-1}) from observations (shaded circles) and simulation of the LU06E06 (shaded).
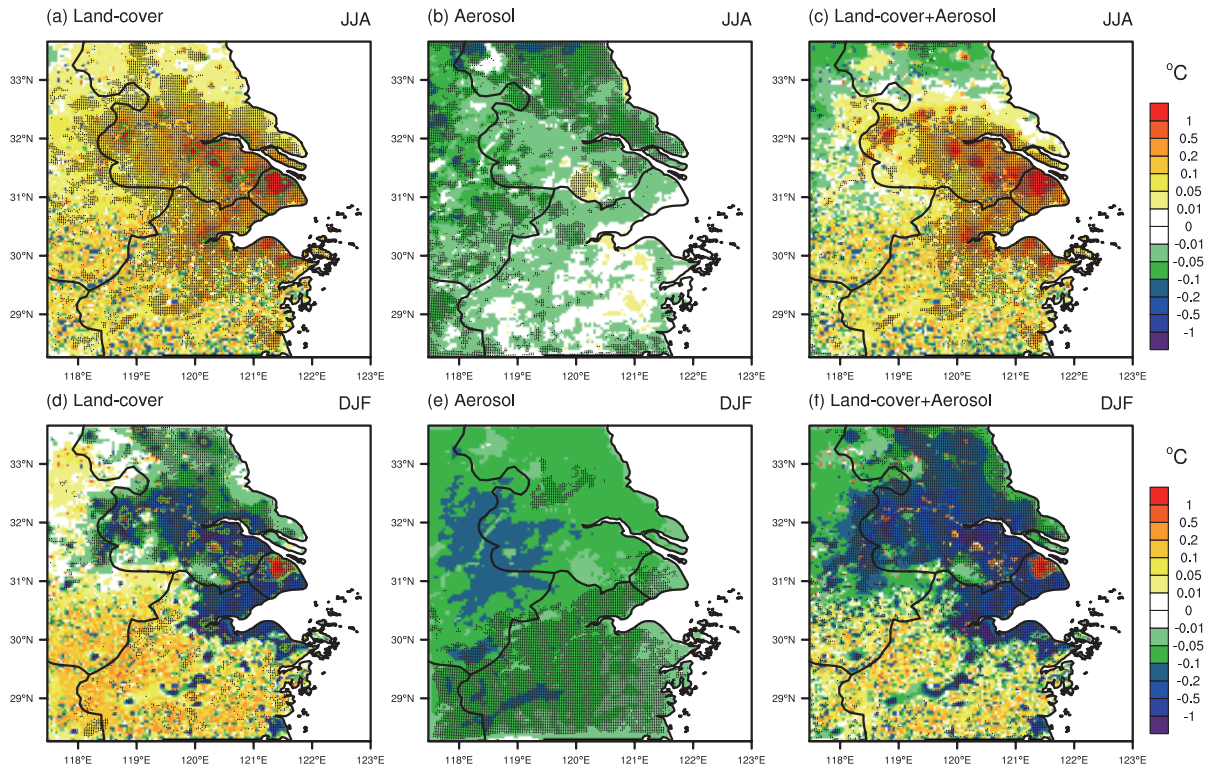
Figure 4 Differences in mean 2-m temperature (Units: °C) between simulations (a, d) LU06E70 and LU70E70, (b, e) LU70E06 and LU70E70, (c, f) LU06E06 and LU70E70 for summer (upper panels) and winter (bottom panels). "Commercial/Industrial/Transportation" areas are marked with green lines. The black dots mark the area with statistically significant changes.
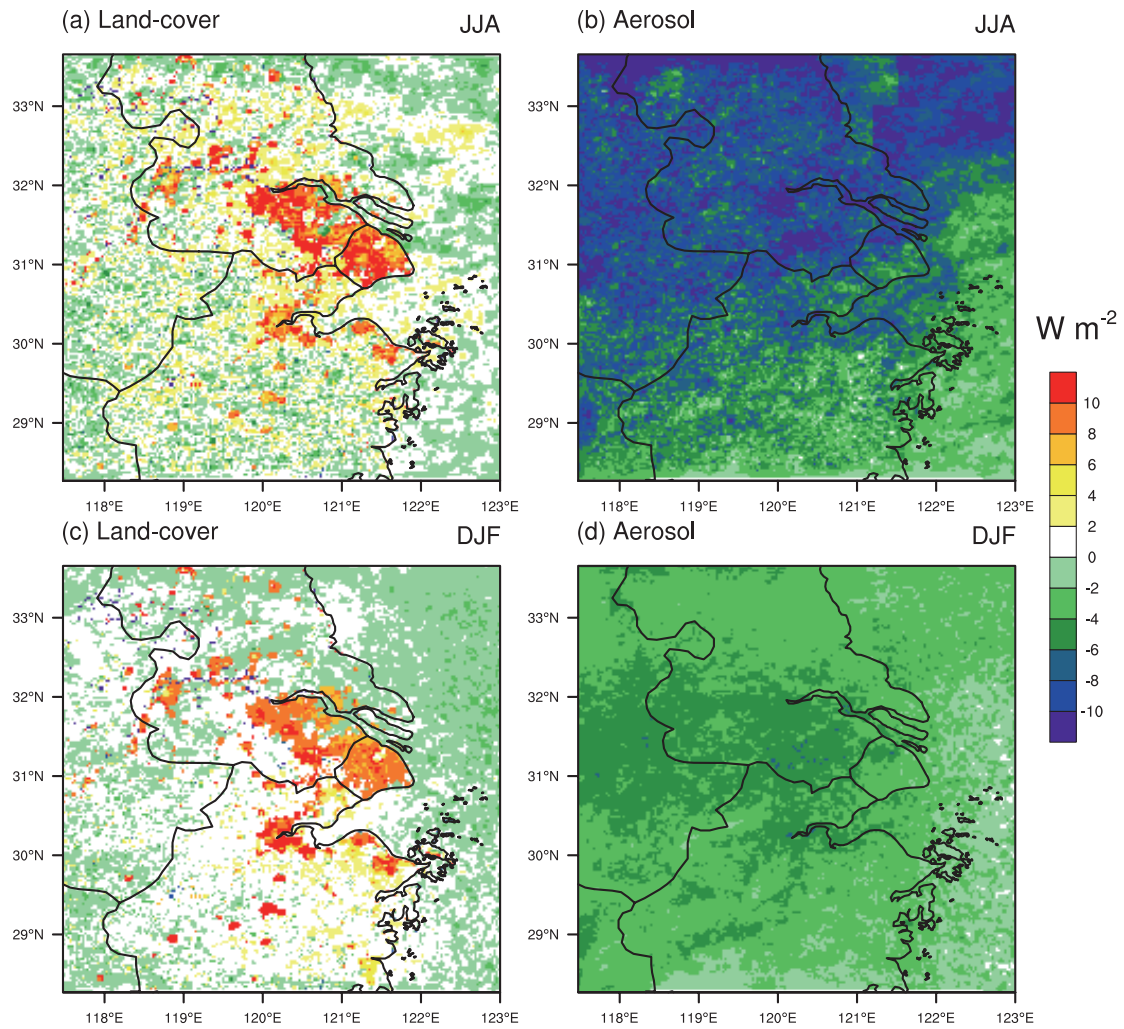
Figure 5 Differences in net shortwave fluxes at the surface (units: W m^{-2}) between simulations (a, c) LU06E70 and LU70E70, and (b, d) LU70E06 and LU70E70 in summer (upper panels) and winter (bottom panels).
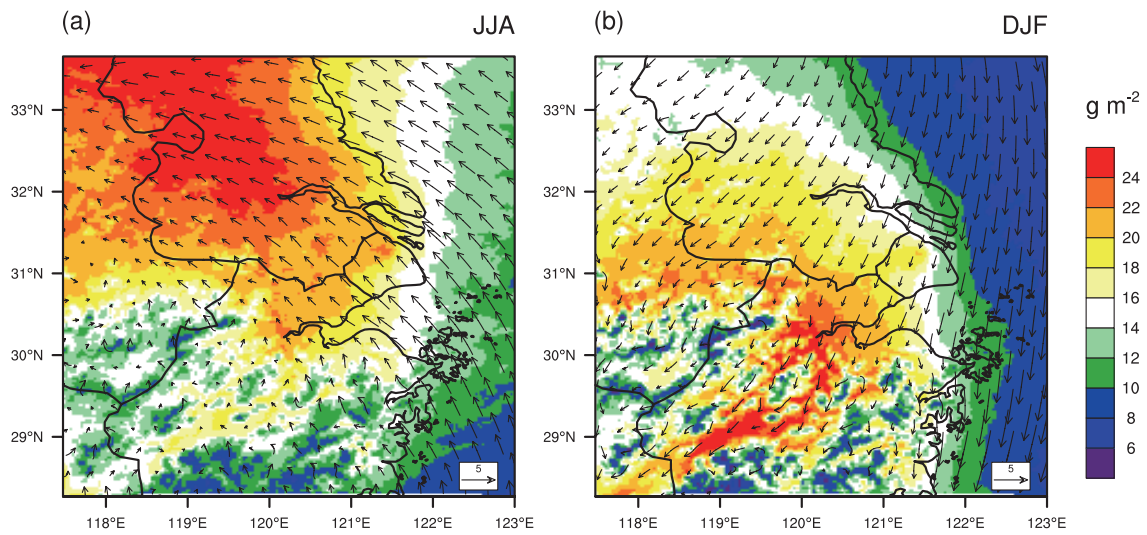
Figure 6 Differences in column burden of PM2.5 (g m^{-2}) between simulations LU70E06 and LU70E70, superimposed with near-surface winds simulated in LU70E70, for (a) summer and (b) winter.
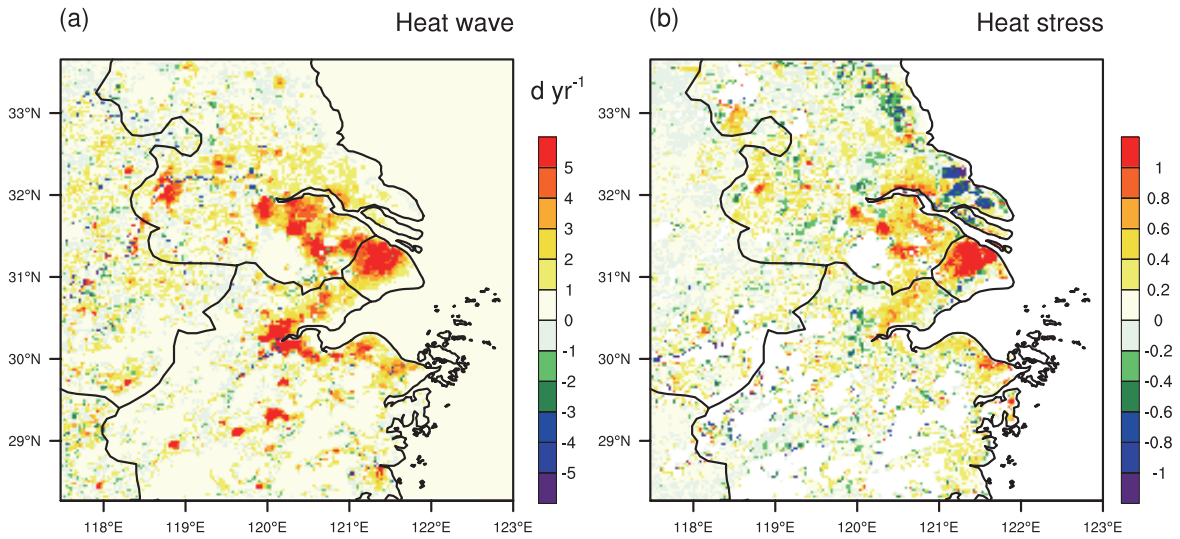
Figure 7 Differences in mean summertime (a) heat wave days (units: d/yr) and (b) heat stress (units: °C) between simulations LU06E70 and LU70E70.
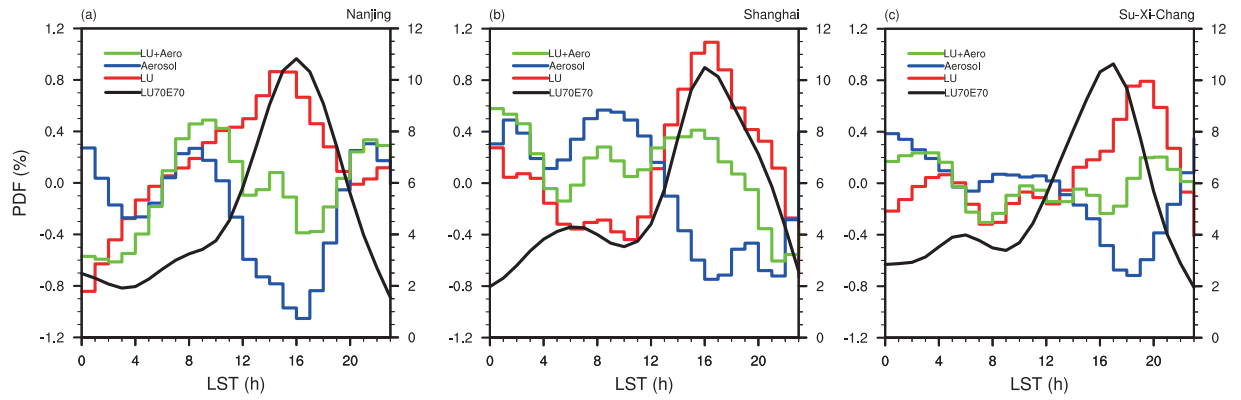
Figure 8 Diurnal cycles of the frequency of summertime extreme rainfall events for LU70E70 (defined using hourly precipitation intensity above 95th percentile, black lines, right axis) and the differences between simulations over (a) Nanjing, (b) Shanghai, and (c) Su-Xi-Chang. Red lines are for land use effect, blue lines for aerosol effect, and green lines for the combined effect.
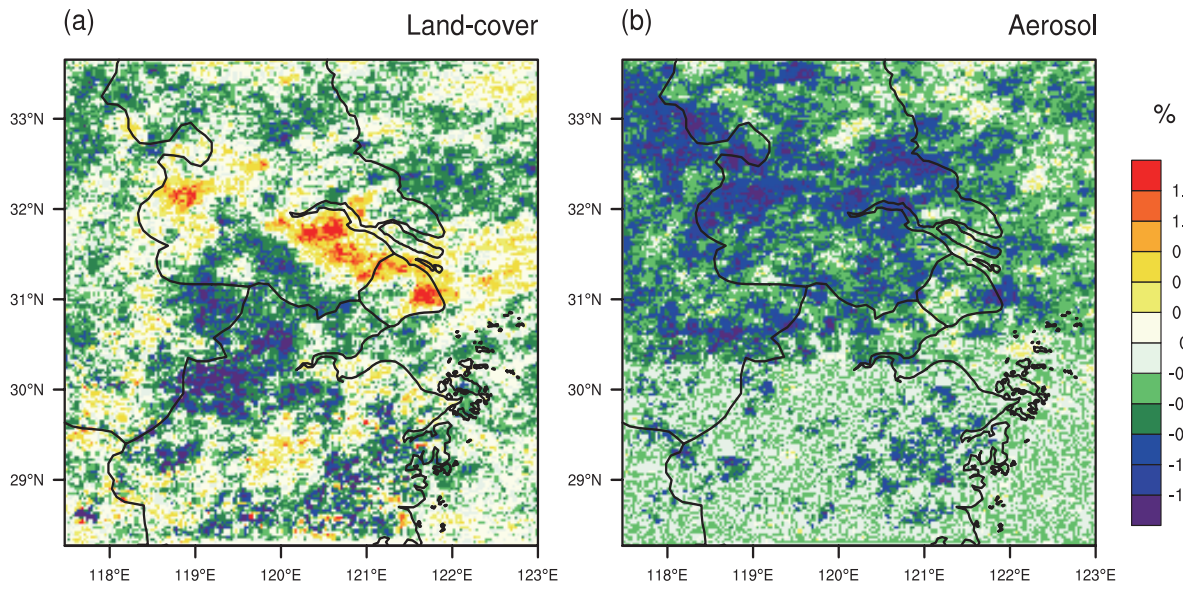
Figure 9 Differences in the frequency of summertime extreme rainfall events (averaged from 12:00 to 20:00 LST) between simulations (a) LU06E70 and LU70E70, and (b) LU70E06 and LU70E70.
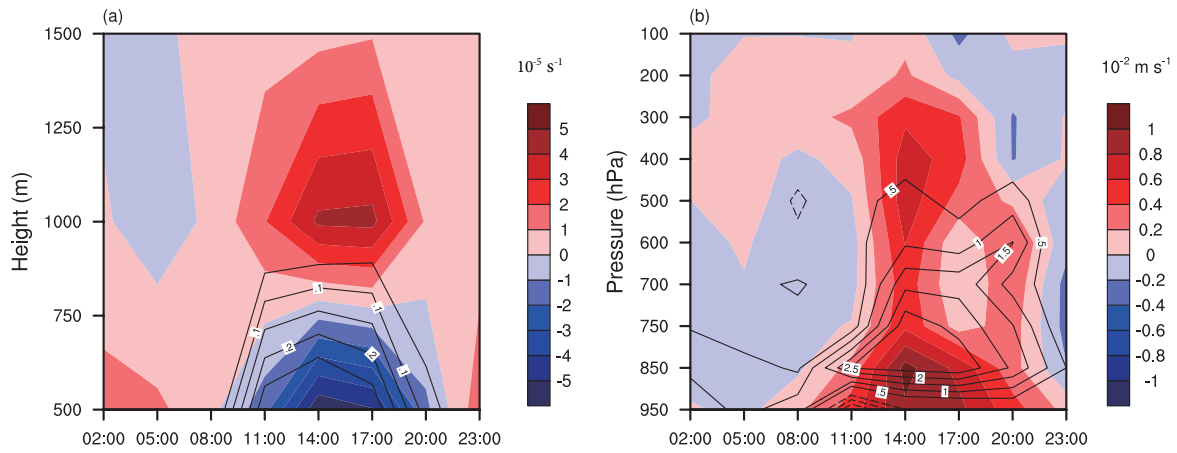
Figure 10 (a) Time-height cross-sections of differences (between LU06E70 and LU70E70) in temperature (contour; units: °C) and divergence (shade; units: 10^{-5} s^{-1}) averaged over the three city clusters (Nanjing, Shanghai, and Su-Xi-Chang); (b) same as (a), but for vertical velocity (shade; units: 10^{-2} m s^{-1}) and cloud water mixing ratio (contour; 10^{-3} kg kg^{-1}).
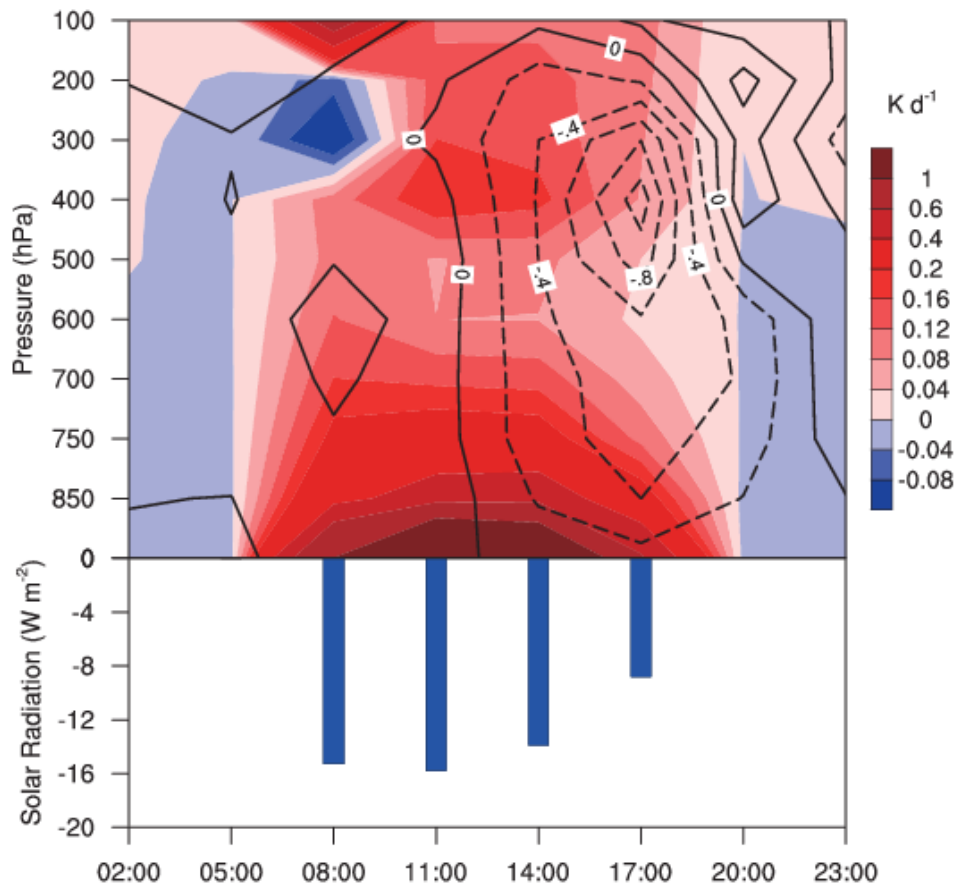
Figure 11 Time-height cross-sections of differences (between LU70E06 and LU70E70) in radiative heating profile (shade; units: K d^{-1}), vertical velocity (contour; units: 10^{-2} m s^{-1}) and surface solar radiation (blue bars; units: W m^{-2}) averaged over the three city clusters (Nanjing, Shanghai, and Su-Xi-Chang).
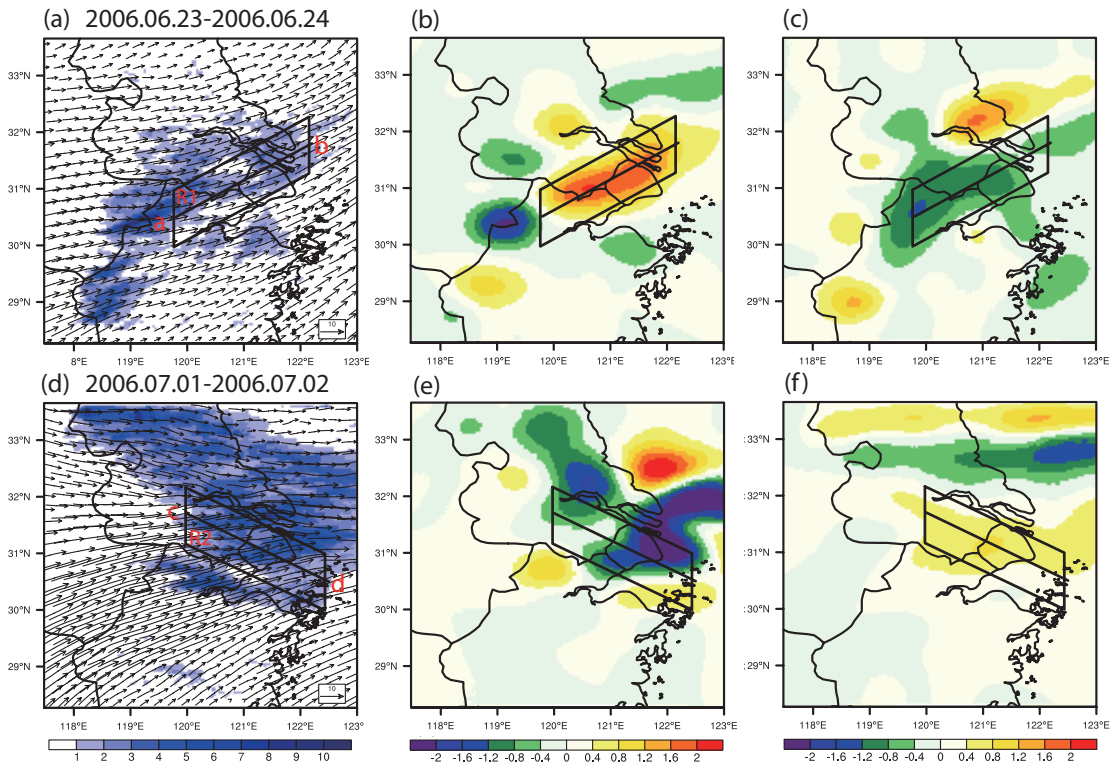
Figure 12 Rain rate (units: mm h-1) superimposed with wind vectors at 850 hPa for case A from 08:00 LST 23 June to 08:00 LST 24 June 2006 (a) simulated in the LU06E06 simulation, (b) differences between LU06E70 and LU70E70, (c) differences between LU70E06 and LU70E70. Panels (d-f) are the same as (a-c) but for case B from 08:00 LST 1 July to 08:00 LST 2 July 2006. The boxes R1 in (a), R2 in (d) outline the three regions over which further analysis are conducted. Lines across the center of each box mark the cross-sections to be analyzed.
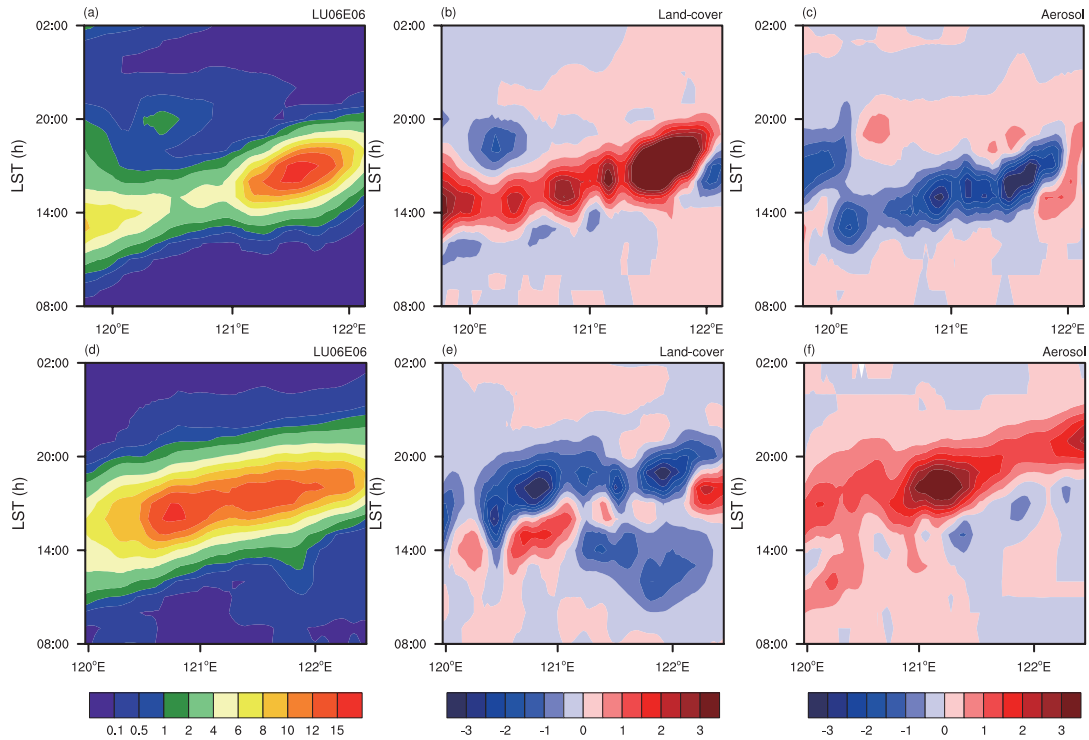
Figure 13 The time evolution of precipitation (units: mm h^{-1}) along the line *ab* (marked in Fig. 12a) from 08:00 LST 23 June to 02:00 LST 24 June 2006 (case A) (a) simulated in the LU06E06 simulation, (b) differences between LU06E70 and LU70E70, (c) differences between LU70E06 and LU70E70. Panels (d-f) are the same as (a-c) but for case B along line *cd* (marked in Fig. 12d) from 08:00 LST 1 July to 02:00 LST 2 July 2006**.**
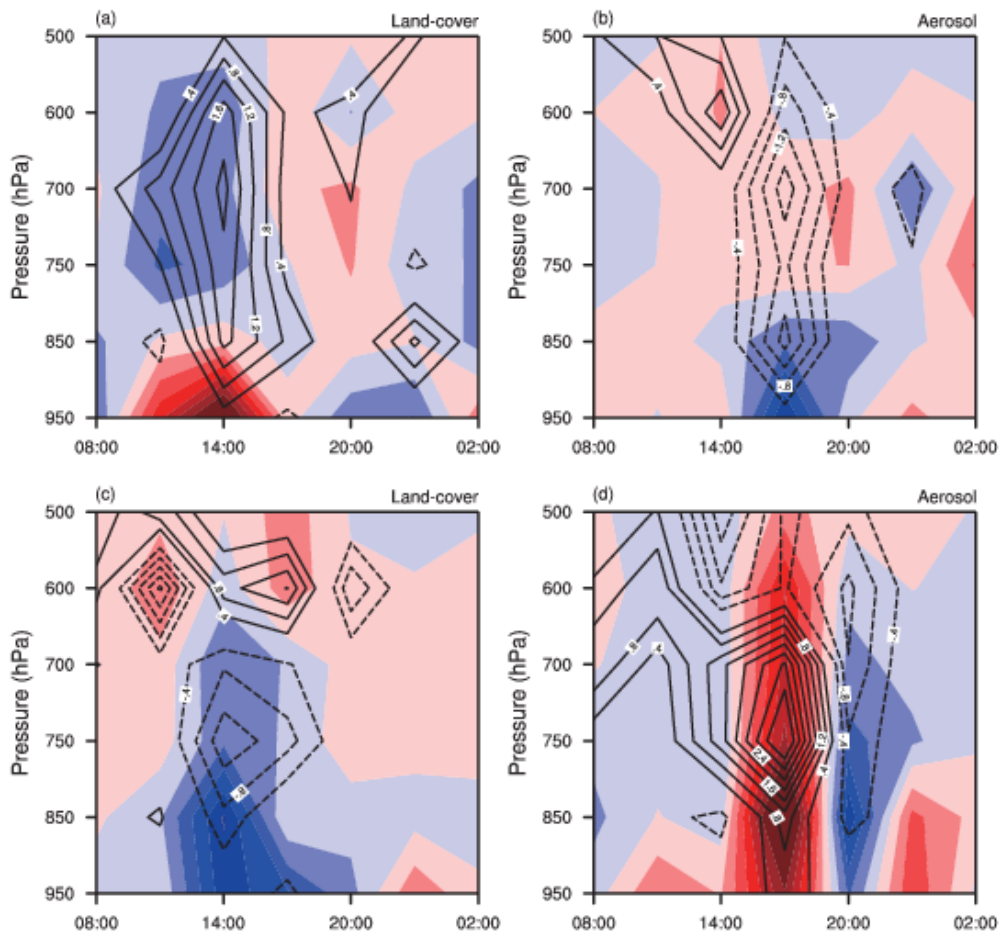
Figure 14 Time-height cross-sections of differences in moisture flux convergence (shaded; units: 10^{-4} g^{-1} kg^{-1} s^{-1}) and water vapor mixing ratio (black lines; units: 10^{-2} g kg^{-1}) from 08:00 LST 23 June to 02:00 LST 24 June 2006 (case A) over region R1 (denoted in Fig. 12a) between (a) LU06E70 and LU70E70; (b) LU70E06 and LU70E70; Panels (c, d) are the same as (a, b) but for case B from 08:00 LST 1 July to 02:00 LST 2 July 2006 over R2 (denoted in Fig. 12d).
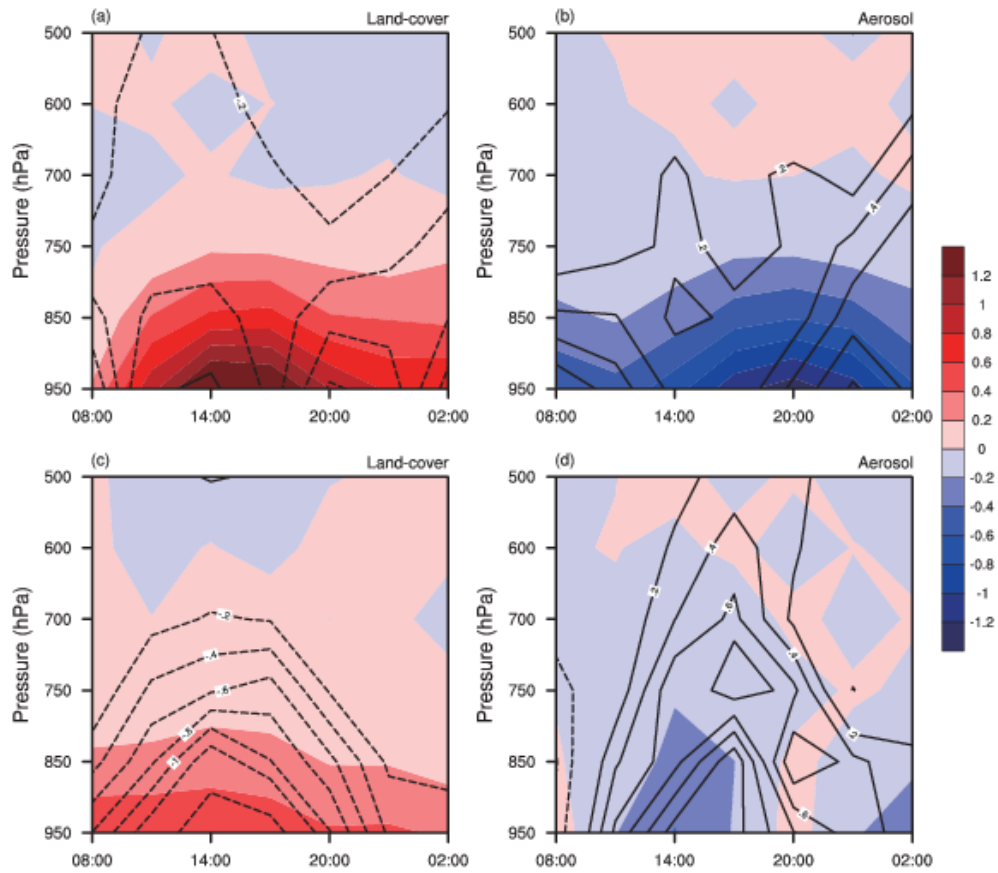
Figure 15 Same as Fig. 14 but for differences in the CON term (shaded; units: $10^{-4}\,g^{-1}kg^{-1}\,s^{-1}$) and MA term (black lines; units: $10^{-4}\,g^{-1}\,kg^{-1}\,s^{-1}$) in eq. (2).
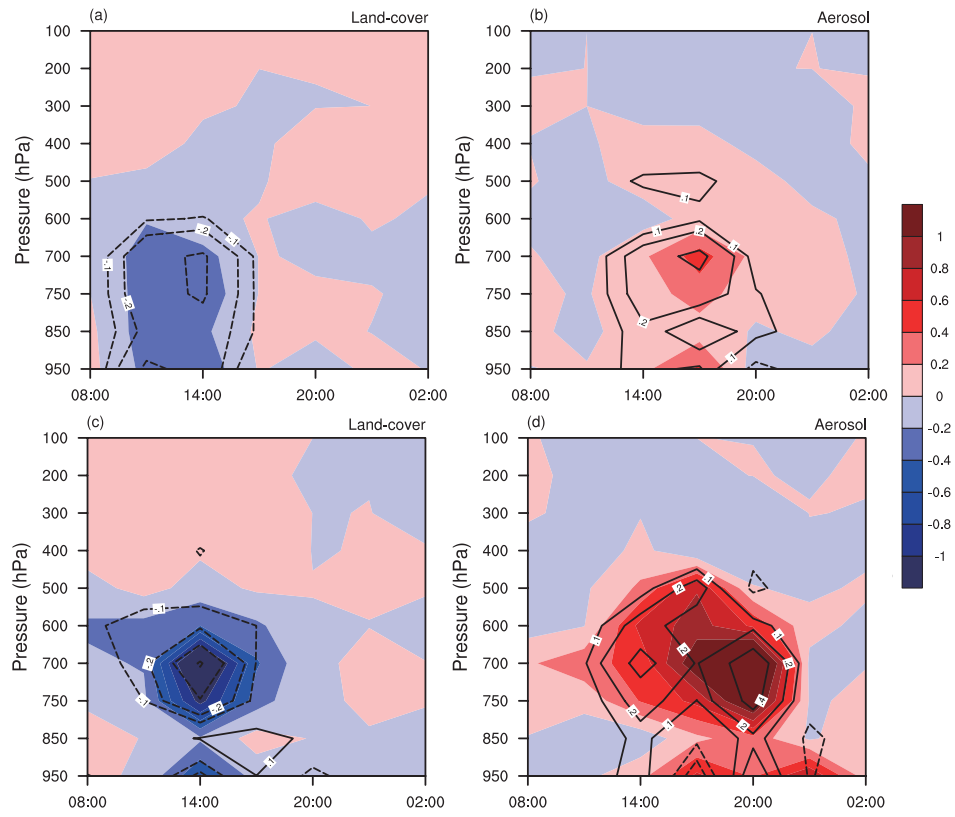
Figure 16 Same as Fig. 15 but for differences in the first term $(-V_{ctrl} \cdot \Delta(\nabla q))$ (shaded; units: 10^{-4} $g^{-1} kg^{-1} s^{-1}$) and the second term $(- (\nabla q)_{ctrl} \cdot \Delta V)$ (black lines; units: $10^{-4} g^{-1} kg^{-1} s^{-1}$) in Eq.3.